THE GROWTH

OF

THIN NICKEL OXIDE FILMS

THE ROLE OF STRUCTURAL DEFECTS

IN THE GROWTH OF

THIN NICKEL OXIDE FILMS

By

JOHN MILLER PERROW, B.Sc., M.Sc.

A Thesis

Submitted to the Faculty of Graduate Studies

in Partial Fulfilment of the Requirements

for the Degree

Doctor of Philosophy

McMaster University

October 1967

DOCTOR OF PHILOSOPHY (1967)
(Metallurgy)

McMASTER UNIVERSITY
Hamilton, Ontario.

TITLE: The Role of Structural Defects in the Growth of Thin Nickel Oxide Films

AUTHOR: John Miller Perrow, B.Sc. (McMaster University)
M.Sc. (McMaster University)

SUPERVISOR: Professor W. W. Smeltzer

NUMBER OF PAGES: ix, 89

SCOPE AND CONTENTS:

In this thesis, the nature and distribution of the structural defects present in thin nickel oxide films formed at 500° and 600°C have been determined, as a function of oxidation time, by means of transmission electron microscopy. For nickel oxide films of thicknesses up to at least 3500 and 5000Å, formed at 500° and 600°C respectively, the films were relatively uniform in thickness on individual metal grains and were composed of small oxide crystallites. The increase in crystallite size with oxidation time has been related to recrystallization and grain growth processes occurring in the films. An oxide film model has been advanced correlating the oxidation kinetics and simultaneous lattice diffusion and short-circuit diffusion via crystallite boundaries.

At a later stage of growth the films consisted of large oxide grains containing randomly distributed dislocations or well defined sub-boundaries. These films exhibited non-uniform growth which has been attributed to the short-circuit diffusion of nickel via dislocations or sub-boundaries oriented approximately perpendicular to the plane of the film.

ACKNOWLEDGEMENTS

Grateful acknowledgement is made to Dr. W. W. Smeltzer for suggesting the problem and for his continuing direction and guidance throughout all stages of this project.

The author is indebted to Dr. R. K. Ham for his help in interpreting the electron microscopy results, and especially to Dr. J. D. Embury for suggesting the use of dark field microscopy and his many helpful discussions concerning the analysis of the experimental data.

The author wishes to thank the staff and graduate students of the McMaster Metallurgy Department for their help and stimulating discussions. In particular, thanks are due to Mr. R. Foster for his help with the construction of the experimental apparatus; and to Mr. H. Walker for his assistance in electron microscopy.

The nickel used in this investigation was supplied through the courtesy of the Falconbridge Nickel Mines Metallurgical Laboratory, Thornhill, Ontario.

This project was supported by grants from the U.S. Air Force Office of Scientific Research, Air Research and Development Command, to Dr. W. W. Smeltzer, and a Steel Company of Canada Fellowship in Metallurgy, and National Research Council of Canada Graduate Studentships awarded to the author.

TABLE OF CONTENTS

	Subject	Page
ACKNOWLEDGEMENTS		(iii)
CHAPTER I	Introduction	1
CHAPTER II	Literature Review	3
2.1	The Oxidation of Metals	3
2.1 (i)	Oxide Defect Structures	3
2.1 (ii)	Oxidation Rate Laws	4
2.1 (iii)	Effect of Temperature and Pressure	5
2.2	Oxidation Mechanisms	6
2.2 (i)	Thin Oxide Films	6
2.2 (ii)	Thick Oxide Films	8
2.3	Grain Boundary and Dislocation Diffusion in Oxide Films	9
2.4	Grain Boundary and Dislocation Diffusion	10
2.5	The Oxidation of Nickel	12
CHAPTER III	Theoretical Considerations	17
3.1	Oxide Film Model	17
3.2	Analysis of Experimental Data	20
3.3	Assessment of the Film Model	25
CHAPTER IV	Experimental Apparatus and Procedure	26
4.1	Sample Material and Surface Preparation	26
4.2	Oxidation Apparatus	26
4.3	Oxidation Procedure	30
4.4	Stripping of the Oxide Films	31

	Subject	Page
4.5	Oxide Surface Replicas	31
4.6	The Electron Microscope	32
CHAPTER V	Experimental Results	33
5.1	Surface Preparation	33
5.2	Oxidation Kinetics	35
5.3	Transmission Electron Microscopy	35
5.3 (i)	General Features	35
5.3 (ii)	Dark Field Electron Microscopy	39
5.4	Crystallite Size Distribution	42
5.5	Dislocation Structures	47
CHAPTER VI	Discussion	61
6.1	General Discussion	61
6.2	Recrystallization and Grain Growth	64
6.3	Correlation of Oxidation Kinetics with Film Structure	67
6.3 (i)	Oxide Film Model	68
6.3 (ii)	Analysis of Data for Oxidation Kinetics	71
6.3 (iii)	The Growth of Non-Uniform Oxide Films	79
CHAPTER VII	Suggestions for Further Work	81
CHAPTER VIII	Conclusions	83
BIBLIOGRAPHY		85

LIST OF ILLUSTRATIONS

Figure	Subject	Page
1	Relationship between the parabolic rate constant and reciprocal temperature for nickel	14
2	Oxidation kinetics for nickel over the temperature range 550°-850°C. Curves calculated by equation (18)	21
3	Relationship between the parabolic rate constant and reciprocal temperature for nickel	23
4	Plots of log $f^{\circ}\alpha$ and log k versus 1/T for nickel	24
5	A schematic diagram of the oxidation apparatus	29
6	NiO film formed on a chemically polished surface (nitric and water)	34
7	NiO film formed on a chemically polished surface (nitric and methanol)	34
8	NiO film formed on an electrochemically polished surface (nitric and methanol)	34
9	NiO film formed on a mechanically polished surface (600 grit)	34
10	NiO film formed on a mechanically polished surface (0.3 u)	36
11	Oxidation kinetics for nickel at 500° and 600°C	37
12	An 1800Å NiO film formed at 500°C	38
13	A 1300Å NiO film formed at 600°C	38
14	A 1300Å NiO film formed at 600°C	38

Figure	Subject	Page
15	A 700Å NiO film formed at 500°C	38
16	Increase in crystallite size with increased film thickness	40
17	Replicas of oxide films	41
18	Bright and dark field of a 700Å NiO film formed at 500°C	43
19	Bright and dark field of a 1000Å NiO film formed at 500°C	43
20	Bright and dark field of a 1300Å NiO film formed at 500°C	44
21	Bright and dark field of a 1700Å NiO film formed at 500°C	44
22	Bright and dark field of a 600Å NiO film formed at 600°C	45
23	Bright and dark field of a 1300Å NiO film formed at 600°C	45
24	Bright and dark field of a 2600Å NiO film formed at 600°C	46
25	Crystallite size distribution at 500°C	48
26	Crystallite size distribution at 600°C	49
27	Average crystallite size versus oxidation time	50
28	Average crystallite size versus film thickness	51
29	Dislocations in a NiO film	53
30	Light transmission of an extremely uneven NiO film	53
31	Electron transmission of an extremely uneven NiO film	53

Figure	Subject	Page
32	An 8000Å NiO film formed at 600°C	54
33	Replica of an extremely uneven NiO film	54
34	Dislocation networks in a NiO film	55
35	Sub-grains in a NiO film	56
36	Example of Kikuchi line shift	58
37	Dislocations in a NiO film	59
38	NiO films formed at 800°C	59
39	$D_t^2 - D_o^2$ versus oxidation time	66
40	Parabolic plots for oxidation of nickel at 500° and 600°C	72
41	Oxidation kinetics for nickel at 500°C	77

LIST OF TABLES

Table	Subject	Page
I	Spectrographic analysis of nickel	27
II	Calculated values for D_B/D_L and E_B/E_L	74
III	Measured versus calculated crystallite size	75

CHAPTER I

Introduction

Almost all metals are thermodynamically unstable when exposed to oxygen, generally resulting in the formation of a compact oxide film on the surface of the metal. This film separates the metal from the oxygen and in order for the reaction to continue at least one of the reactants must be transported across the film. Many investigations have shown that at sufficiently high temperatures most metals oxidize according to a parabolic rate equation for oxide films greater than 10,000Å in thickness. The universally accepted rate controlling mechanism for parabolic oxidation is the thermally activated lattice diffusion of metal or oxygen ions across the oxide film.

For the growth of thin oxide films, preceding parabolic behaviour, many metals oxidize too rapidly to be explained by lattice diffusion. Consequently, several investigators have advanced the hypothesis that the rapid growth of thin oxide films occurs by lattice diffusion and diffusion along low resistance paths such as pores, dislocations or oxide crystallite boundaries. To date, however, no direct correlation has been obtained between structural defects and oxidation kinetics.

In the present investigation the techniques of transmission electron microscopy were employed to determine the nature and distribution of the structural defects present in thin nickel oxide films as a function of oxidation time. Nickel was specifically chosen for this

investigation for a number of very important reasons. The oxidation of nickel results in the formation of a compact, adherent oxide film consisting solely of face centered cubic NiO. The solubility of oxygen in nickel is low and the coefficients of thermal expansion for nickel and nickel oxide are almost identical. In addition, considerable data is available in the literature concerning the oxidation kinetics of nickel and the self-diffusion of nickel in nickel oxide.

In this thesis the experimental results are presented following a review of metal oxidation and publications pertinent to this investigation. The observed structural defects are then correlated with lattice and short-circuit diffusion of nickel in nickel oxide to explain the morphological development of the films, and to advance an oxide film model accounting for the observed oxidation kinetics.

CHAPTER II

Literature Review

2.1 The Oxidation of Metals

Since it is technologically important to control the oxidation of metals, many investigations have been carried out aimed at determining oxidation mechanisms and their rate controlling steps. The majority of these investigations have been kinetic studies and a variety of mechanisms have been proposed based primarily on the analyses of kinetic data. The more important of these are briefly reviewed in this chapter and the reader is referred to the reviews of Evans(1), Kubaschewski and Hopkins(2), Hauffe(3) and Benard(4) for greater detail.

2.1 (i) Oxide Defect Structures

Most metal oxides are semiconductors, their conductivity being mainly electronic rather than ionic, and occurring by the migration of electron holes (p-type or metal deficit semiconductors) or electrons (n-type or metal excess semiconductors). The oxidation rate, however, is generally controlled by the diffusion rate of ions across the oxide film. Therefore, in order to determine the oxidation mechanism of a metal it is necessary to know the defect structure of its oxide.

Metal deficit oxides contain vacancies in the cation sublattice which, in growing oxide films, are formed at the oxide/oxygen interface and consumed at the metal/oxide interface. There is also an equivalent number of positive holes, which are ions in higher valence states, in order to maintain electrical neutrality. In this case cations and

electrons migrate from the metal/oxide interface to the oxide/oxygen interface, via cation vacancies and positive holes respectively, with the diffusion of cations controlling the rate of the oxidation reaction.

Metal excess oxides are of two types; those containing metal ions in interstitial position and those containing vacancies in the anion sublattice. In oxide films of the former type, metal ions diffuse outward from the metal/oxide to the oxide/oxygen interface via an interstitial diffusion mechanism; in the latter type, oxygen ions diffuse inward via anion vacancies. In both cases electrons diffuse from the metal/oxide interface to the oxide/oxygen interface.

2.1 (ii) Oxidation Rate Laws

The large number of studies made of oxidation kinetics have led to a number of empirical relationships which are often referred to as, "oxidation rate laws". These so-called oxidation rate laws are listed here in terms of x, the oxide film thickness, t, the time and K the rate constant:

$$x = K_{li}t; \quad \text{the linear rate law} \tag{1}$$

$$x^2 = K_p t; \quad \text{the parabolic rate law} \tag{2}$$

$$x^3 = K_c t; \quad \text{the cubic rate law} \tag{3}$$

$$1/x = A - K_{il} \ln t; \quad \text{the inverse logarithmic rate law} \tag{4}$$

$$x = K_e \ln(at + t_o); \quad \text{the logarithmic rate law} \tag{5}$$

Although oxidation rate equations alone are not sufficient for identifying oxidation mechanisms they do classify the oxidation behaviour

and limit the number of possible mechanisms.

2.1 (iii) Effect of Temperature and Pressure

Temperature and pressure are two reaction variables which can be closely controlled and their effects on the reaction kinetics are often useful in identifying a reaction mechanism.

The temperature coefficient of an oxidation rate constant is often found to obey the familiar Arrhenius equation,

$$K = K_o e^{-Q/RT} \tag{6}$$

where K is the rate constant, K_o is a constant, Q is the activation energy of the rate controlling step, R is the gas constant and T is the absolute temperature. The activation energy is obtained by plotting ln K versus 1/T, the slope of which is -Q/R. Comparing the activation energy obtained in this manner with those of suspected rate controlling steps can assist in identifying the rate controlling process. If the Arrhenius plot shows a change in slope it usually means that there has been a change in the rate controlling process or in the physical properties of the oxide film.

The effect of oxygen pressure on the oxidation kinetics is essential in evaluating the rate determining process. If absorption is a rate determining factor, the reaction normally exhibits a large oxygen pressure dependence. At low pressures (<1 torr) the reaction rate is proportional to the impingement rate of oxygen molecules, and is directly proportional to the oxygen pressure. At high oxygen pressures, oxidation rates are often found to be proportional to the square root of pressure. This relationship suggests that the dissociation of

oxygen on the oxide surface is rate controlling.

If a diffusion process is rate controlling, a pressure effect can arise due to the effect of pressure on the concentration of defects at the oxide/oxygen interface. In the case of n-type oxides, the concentration of defects is considered to be negligible at the oxide/oxygen interface and no pressure dependence is observed. For p-type oxides, a pressure dependence is observed which is related to the defect structure of the oxide.

2.2 Oxidation Mechanisms

Oxidation mechanisms are generally divided into two groups relating to the formation of thin and thick oxide films respectively. This division is arbitrary but not without basis since different oxidizing conditions and experimental techniques are employed in investigating the two cases, often permitting secondary factors to become significant. In this brief review of oxidation mechanisms, the division between thin and thick films is made on the basis of the different driving forces responsible for film thickening as proposed by Seybolt(5). For thick films, the driving force is the concentration gradient existing across the film which thickens as a result of the thermally activated diffusion of reactants. For thin films, the driving force is the electrical field existing within or across the film arising from the interaction of electrons from the metal and absorbed oxygen atoms.

2.2 (i) Thin Oxide Films

This classification refers to the oxide films formed at low temperatures where thermally activated diffusion is negligible. A characteristic feature of low temperature oxidation is a very rapid initial reaction rate which decreases to a low level once the oxide film

has reached a thickness of several hundred Ångstroms or less. The oxidation kinetics usually conform to a logarithmic, inverse logarithmic or a cubic rate equation. While a number of mechanisms have been proposed for the growth of thin oxide films, none have received general acceptance.

Mott(6) proposed a model in which electron tunnelling through very thin films is rate determining and derived a logarithmic rate equation. Hauffe and Ilschner(7) followed the same concept and elaborated on this model. In a later study Cabrera and Mott(8) proposed that mobile cations could be pulled through a thin oxide film by the strong electric field generated by electrons diffusing from the metal to the oxygen atoms absorbed at the oxide surface. This model led to an inverse logarithmic rate equation for films less than 80Å, a parabolic equation for n-type films less than 1000Å and a cubic equation for p-type films less than 1000Å. Grimley and Trapnell(9) proposed that instead of a constant potential existing across the film, as assumed by Cabrera and Mott(8), an electrical field of constant intensity existed within the film. On this basis, linear rate equations were obtained for n-type oxide films if surface reactions or transport of metal ions via interstitial positions were rate determining. For p-type films, logarithmic and cubic rate equations were derived when the rate controlling steps were cation diffusion and the formation of cation vacancies at the oxide/oxygen interface, respectively.

More recently Uhlig et al(10) considered the effects of electrical space charge distributions within the oxide film. By assuming that the transfer of electrons from the metal to the oxide is rate

determining he derived a two stage logarithmic rate equation. Landsberg[11] assumed that the chemisorption of oxygen is rate determining and derived a logarithmic rate equation.

While the above mechanisms have successfully described the oxidation behaviour of a particular metal in a particular environment, none are generally applicable. Furthermore, the same rate equation can be derived using different assumptions making it extremely difficult to draw definite conclusion concerning the oxidation mechanism of thin oxide film formation at low temperatures.

2.2 (ii) Thick Oxide Films

This classification refers to films greater than 10,000Å in thickness. These films, which are assumed to be electrically neutral, form very rapidly at high temperatures and only after extended periods of time at intermediate temperatures. In most cases, thick oxide films exhibit parabolic growth behaviour but occasionally linear growth kinetics are observed which are attributed to either a phase boundary-controlled reaction or breakdown and spalling of the oxide film from the metal[2].

Tammann[12] and Pilling and Bedworth[13] were the first investigators to recognize the parabolic oxidation behaviour of metals. They postulated that the rate controlling step was the diffusion of reactants across the oxide film but did not specify the nature of the diffusing species. In 1933 Wagner[14] formulated a quantitative theory for the parabolic growth of thick oxide films which has since been tested and verified by numerous investigators. Wagner assumed that ions and electrons, which migrate independently of one another, are the only diffusing species. The prerequisite for an ionic species to be mobile is that

its sublattice be defective. Reactions at phase boundaries are considered to be sufficiently rapid for local equilibria to exist at the oxide/oxygen and metal/oxide interfaces. On the basis of these assumptions, Wagner derived an expression for the reaction rate in terms of electrical conductivity and the transference numbers of the cations, anions, and electrons.

Wagner[15] also obtained an alternative useful expression utilizing ion mobilities, which are generally easier to determine than transference numbers, and can be expressed in terms of self diffusion constants of the ions, namely

$$Kr = C_i \int_{a_X^{(m)}}^{a_X^{(s)}} \left(D_c \frac{Z_c}{Z_X} + D_X\right) d \ln a_X \tag{7}$$

where $C_i = Z_c C_c = Z_X C_X$ is the concentration of metal or non-metal ions in the oxide in equivalents per cubic centimeter, a_X is the thermodynamic activity of the non-metal, and D_c and D_X are the self diffusion coefficients of the metal and non-metal respectively.

2.3 Grain Boundary and Short-Circuit Diffusion in Oxide Films

In all of the oxidation mechanisms described previously, it is assumed that the oxide film is homogeneous and does not contain structural irregularities such as pores, grain boundaries or dislocations. Investigations on the nucleation of oxide metal surfaces[16,17,18] and transmission electron microscopy of thin oxide films[19,20,21] have shown that this assumption may be an over simplification. Furthermore, diffusion studies on polycrystalline materials[22] have shown that such structural defects act as low resistance diffusion paths and may be an

important mode of transportation, especially at intermediate temperatures.

Evans[23] and Davies et al[24] have proposed models where transport of reactants is assumed to take place preferentially along pores or low resistance diffusion paths. Two cases were considered. In the first, fresh oxide results in self-blockage of pores and an asymptotic oxidation rate; in the second case, mutual blockage occurs due to compressive stresses and a logarithmic oxidation rate is observed. Harrison[25] recently has derived an expression which accounts for self-and mutual blockage occurring simultaneously.

Meijering and Verheijke[26] observed a cubic rate for the oxidation of cuprous to cupric oxide at 800° to 1000°C and interpreted this in terms of a change in permeability of the cuprous oxide layer with time. The exact nature of the ageing of the oxide was not established. Using a more refined oxide film model to account for a change in permeability with time, Smeltzer et al[27] proposed a theory to describe the non-parabolic oxidation kinetics of titanium, hafnium and zirconium. In this theory, lattice diffusion and diffusion along low resistance paths, which decrease in density with time, were assumed to occur simultaneously. More recently, Irvine[28] proposed a model for non-parabolic oxidation based upon a combination of diffusion along grain boundaries and lattice diffusion. The contribution of grain boundary diffusion to the effective diffusion coefficient was weighted according to the oxide grain size.

2.4 Grain Boundary and Dislocation Diffusion

As illustrated in the above section, investigators are beginning to consider the role of grain boundary and dislocation or short-

circuit diffusion in the transport of reactants in oxide films. Since this present investigation is concerned with these factors, a brief review is presented of published diffusion analyses.

Mathematical solutions for grain boundary diffusion have been presented by Fisher[29] and Whipple[30] in which the grain boundary is assumed to be a narrow region having a high rate of diffusion compared to the adjacent grains. In this model, material is assumed to diffuse rapidly along the grain boundaries and to diffuse concurrently by lattice diffusion into the grains. By making the further assumption that the concentration of the diffusing material remains constant at the original interface, approximate solutions for the concentration profile have been derived.

Turnbull and Hoffman[31] interpreted enhanced grain boundary diffusion in tilt boundaries in terms of a dislocation pipe model. The boundary was regarded as a wall of equidistant edge dislocations, and it was assumed that preferential grain boundary diffusion took place along the dislocation pipes. The dependence of diffusion on grain misorientation was accounted for in terms of the change in number and spacing of dislocation pipes.

Hart[32] has derived an expression for enhanced diffusion in a crystal containing a large number of dislocation short-circuiting pipes in terms of a random walk model and gives the expression

$$D_{obs} = D_L(1-f) + D_d f \tag{8}$$

where D_{obs} is the observed or measured diffusion coefficient, D_L and D_d are the lattice and dislocation diffusion coeffients respectively, and f is the fraction of atoms in dislocations. This result was arrived

at by assuming that the diffusing atoms spend a significant amount of time in the region of dislocations where the diffusivity is orders of magnitude greater than in the bulk. Rouff and Balluffi[33] have shown that if the dislocations are stationary then a necessary condition for the Hart relationship to hold is $2(D_L t)^{1/2} > l_d$ where l_d is the dislocation spacing. When this condition fails, the amount of short-circuiting is greatly reduced and the dislocations become essentially "clogged". However, if the dislocations move through the crystal, as they do in plastic deformation, the dislocations may visit the diffusing atoms. In such cases, the short-circuiting may again be randomized and enhanced diffusion occur.

2.5 The Oxidation of Nickel

The oxidation behaviour of nickel has been extensively investigated over a wide range of temperatures and pressures, not only because nickel is a technologically important metal, but also because the nickel-oxygen system has a number of properties which makes it particularly attractive for the study of oxidation mechanisms. Wood et al[34] have recently presented an extensive review on this subject.

When nickel, which is a face centered cubic metal[35], is exposed to oxygen, a compact, adherent, non-volatile oxide film is formed which consists solely of face centered cubic NiO[36,37,38]. The solubility of oxygen in nickel is low, being 0.044 atomic per cent at 1000°C[39], and the coefficients of thermal expansion for nickel and NiO are almost identical with a difference in expansion of only 0.05% on heating from 25° to 1000°C. Electrical and thermoelectrical studies [41,42] have shown that NiO is a metal deficit semiconductor containing

cation vacancies and positive holes. These defects, which are formed at the NiO/O_2 interface, diffuse inwards and are annulled at the Ni/NiO interface. The most recent experiments on the effect of oxygen pressure on the oxidation of nickel[43] and the electrical conductivity of NiO[44] have shown that the cation vacancies are singly ionized. The defect equation for nickel oxidation is therefore written:

$$1/2O_2 + Ni^{+2} = Ni_{\square}^{+} + \oplus \qquad (9)$$

Furthermore, on the basis of diffusion measurements of nickel[45,46,47 48], and of oxygen[49] in NiO it can safely be assumed that nickel ions are the predominant diffusing species.

The majority of the oxidation studies carried out on nickel have been concerned with the growth of thick oxide films formed in the temperature range 400° to 1400°C. In this case, nickel oxidizes according to a parabolic rate equation[34] and the parabolic rate constants obtained by the various investigators are shown plotted against 1/T in Figure 1. The diffusion coefficients determined for nickel in NiO are also shown plotted in Figure 1 in terms of parabolic rate constants calculated from the expression derived by Shim and Moore[45], namely:

$$Kp = 2D_{Ni} \qquad (10)$$

where Kp is the parabolic oxidation rate constant and D_{Ni} is the self-diffusion coefficient for nickel in NiO. The differences in the values for the parabolic rate constants seen in Figure 1 have been attributed to differences in nickel purity[50,51] and decrease with increasing purity. There is also evidence that the oxidation rate of nickel is

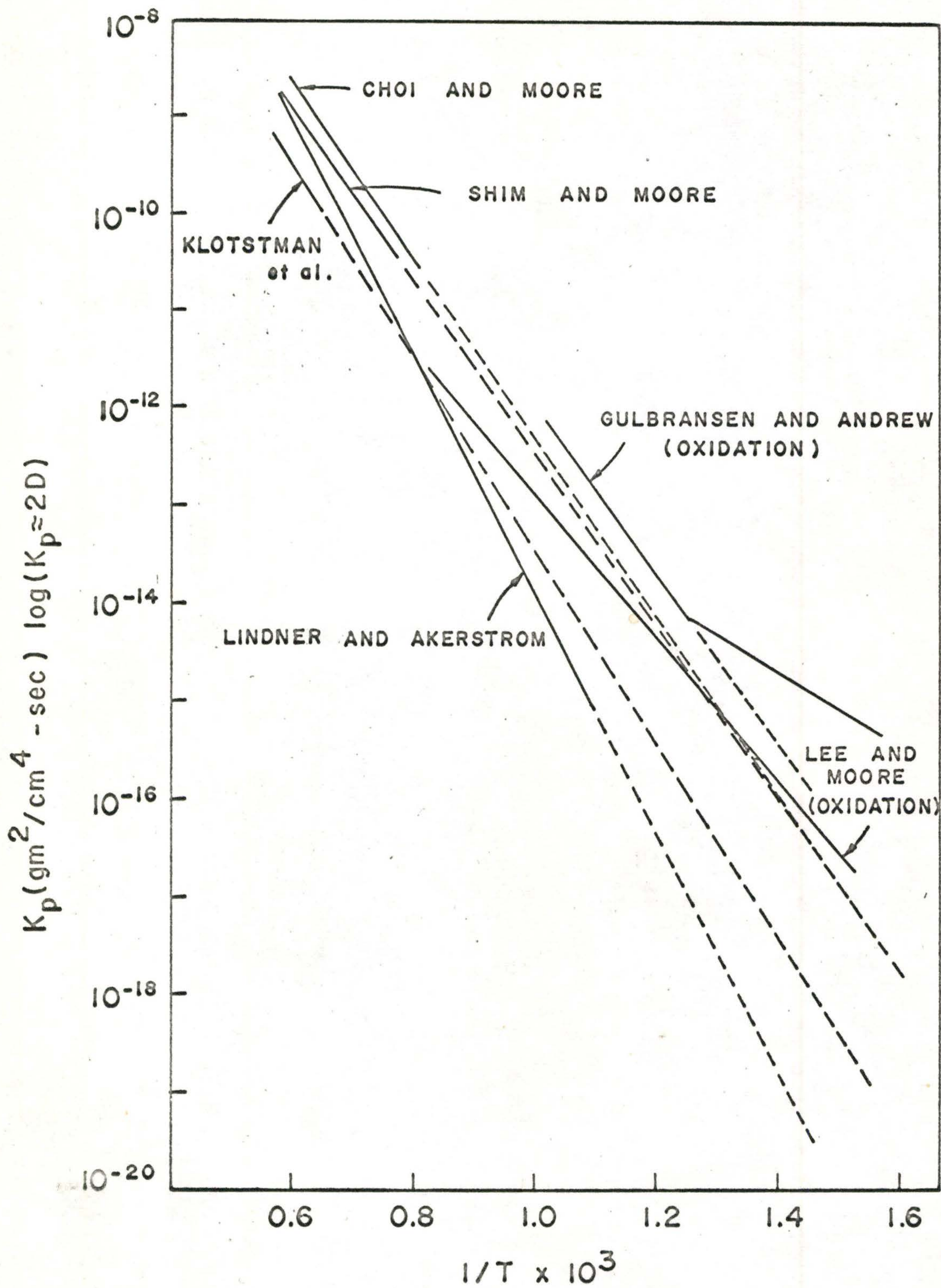

Figure 1: Relationship between the parabolic rate constant and reciprocal temperature for nickel

markedly effected by differences in surface preparation and thermal history of the samples[36].

The growth of thin nickel oxide films of less than 10,000Å in thickness, formed at low temperatures and preceding the formation of thick films at high temperatures, has received little attention. Also, none of the mechanisms which have been proposed by the various investigators have been generally accepted.

At 400°C, Engell et al[53] observed that a cubic rate equation was obeyed. A theoretical expression based on nickel ion diffusion under the influence of an electrical potential gradient was derived to account for this type of oxidation behaviour. Uhlig et al[10] studied the oxidation of nickel in the temperature range 307° to 442°C for film thicknesses up to 3400Å. They found a discontinuity in the oxidation rate at the Curie temperature of 353°C with a good fit to a logarithmic rate equation both above and below this temperature. The authors interpreted their results in terms of electron transfer from metal to oxide being rate controlling. Gulbransen and Andrew[36] investigated the oxidation of nickel in the temperature range 400° to 750°C and observed that at the lower temperatures of 400° to 550°C, the initial oxidation rate was non-parabolic. They offered two explanations for this non-parabolic behaviour. The first was based on the assumption that the concentration of impurities within the oxide was decreasing as the film increased in thickness. This results in a decrease in the number of vacancies available for nickel ion diffusion and a corresponding decrease in the rate of oxidation. The second explanation assumed the occurrence of grain boundary diffusion during the initial stages of

oxidation. As the film thickened, growth of the oxide crystallites occurred until the influence of grain boundary diffusion became negligible compared to lattice diffusion. This second explanation was based on an earlier investigation of Phelps et al[19]. They showed, by means of transmission electron microscopy, that NiO films of less than 500Å in thickness were composed of small crystallites, 300 to 600Å in diameter, which increased in size with oxidation time.

In addition to the above kinetic studies, a number of qualitative investigations of the initial oxidation of nickel are reported in the literature. Martius[54] investigated oxide nucleation at 1100°C in H_2O/H_2 mixtures and observed that the number, shape, and orientation of the nuclei depended upon the orientation of the nickel substrate. The increase in the number of oxide crystallites with increased exposure time was more pronounced than was the increase in crystallite size. Also, the nuclei formed along grain boundaries varied considerably in both number and orientation while no nuclei were observed at twin boundaries. A number of investigators[55,56,57,58,59] have studied the orientation relationship between thin nickel oxide films and the underlying metal. The results of these investigations show that a parallel orientation relationship is the most predominant one for the (100), (110) and (111) orientations of nickel.

CHAPTER III

Theoretical Considerations

In this section, a model is proposed for the oxidation of nickel preceding the onset of parabolic oxidation in the intermediate temperature range 500° to 850°C. This model is formulated from the considerations advanced by Smeltzer et al[27] concerning simultaneous lattice diffusion and diffusion along low resistance paths of decreasing density. An analysis is also present of the extensive kinetic data of Gulbransen and Andrew[36,52] for this temperature range. Although this analysis demonstrates the limitations of the model, several predictions result which indicate the type of experimental data required to develop a more precise model.

3.1 Oxide Film Model

Two processes are envisaged for the outward diffusion of nickel through the film to the oxide/oxygen interface; lattice diffusion and diffusion within a random array of low resistance diffusion paths. The driving force for oxidation is the concentration gradient of nickel between the inner and outer oxide surfaces maintained by the free energy change for oxide formation. A uniform gradient which is inversely proportional to the film thickness is assumed according to the low gradient approximation[14] and interfacial inhibitions are assumed to be negligible.

It has been shown, by transmission electron microscopy, that thin oxide films on nickel are composed of numerous small crystallites which increase in size as oxidation proceeds[19]. The growth of the crystallites decreases the contribution of boundary diffusion to the overall

reaction as suggested by Gulbransen and Andrew[36]. It is assumed as a first approximation in the present model that the time dependence of the fraction of available nickel ion sites within the array of short-circuit paths is governed by the first order rate expression,

$$-\frac{df}{dt} = kf \tag{11}$$

or

$$f(t) = f^{\circ} e^{-kt} \tag{12}$$

Here f° is the initial fraction of total nickel sites within the low resistance paths. The precise decay law chosen is of secondary consequence since k is an adjustable coefficient.

A growth relation for oxide formation may be formulated on the basis of the arguments advanced by Hart[32] for diffusion in solids. As previously reviewed, the effective diffusion coefficient for the movements of atoms in a solid matrix containing a random array of short-circuit paths may be expressed as a weighted sum of coefficients for lattice and boundary diffusion. The effective diffusion coefficient is therefore:

$$D_{eff} = D_L(1-f) + D_B(f) \tag{13}$$

and for the rate of film growth

$$\frac{dx}{dt} = \Omega D_{eff} \frac{\Delta c}{x} \tag{14}$$

In these equations, D_L and D_B are the coefficients for lattice and short-circuit or boundary diffusion of nickel respectively, f is the fraction of total available sites lying within low resistance paths

in the oxide film, Ω is the volume of oxide per nickel ion (cm^3 per ion) and Δc is the concentration difference of nickel ions at the two oxide surfaces (ions per cm^3).

Upon substituation of equations (12) and (13) into equation (14),

$$\frac{dx}{dt} = \Omega \left\{ D_L (1 - f^\circ e^{-kt}) + D_B f^\circ e^{-kt} \right\} \frac{\Delta c}{x} \qquad (15)$$

In the absence of the short circuit diffusion term, equation (15) yields on integration,

$$x^2 = 2 \Omega D_L \Delta c t = K_p t \qquad (16)$$

Equation (16) defines the parabolic rate constant, Kp. In terms of Kp and in the approximation that $D_B \gg D_L$ equation (15) becomes,

$$2x \frac{dx}{dt} = Kp \left\{ 1 + f^\circ \alpha e^{-kt} \right\} \qquad (17)$$

where

$$\alpha = D_B / D_L$$

The growth law for oxidation is obtained by integrating equation (17) to

$$x^2 = Kp \left\{ t + \frac{f^\circ \alpha}{k} (1 - e^{-kt}) \right\} \qquad (18)$$

This equation may now be investigated for various limiting cases which are useful in the analysis of experimental data.

Thin films ($t \rightarrow o$):

$$x^2 = (1+f^\circ\alpha)K_pt \qquad (19)$$

Thick films ($e^{-kt} \ll 1$)

$$x^2 - x^2_o = K_pt \qquad (20)$$

where

$$x^2_o = K_pf^\circ / k \qquad (21)$$

The time t_o at which $x = x_o$ is the solution of

$$e^{-kt_o} \doteq \frac{K_pt_o}{(x_o)^2} \qquad (22)$$

Since t_o is measured and K_p and x_o^2 are known from equation (20), expression (22) yields,

$$k = \frac{1}{t_o} \ln \frac{x_o^2}{K_pt_o} \qquad (23)$$

3.2 Analysis of Experimental Data

This analysis is confined to the kinetic data reported by Gulbransen and Andrew[36,52] for the oxidation of nickel in the temperature range 500° to 850°C shown in Figure 2. The oxidation curves shown were calculated by equation (18) and the parameters K_p and x_o^2 were determined from the slope and intercept of the parabolic asymptote for thick films. The values for k and f° were then determined from equations (23) and (21) respectively. The values for parabolic constants

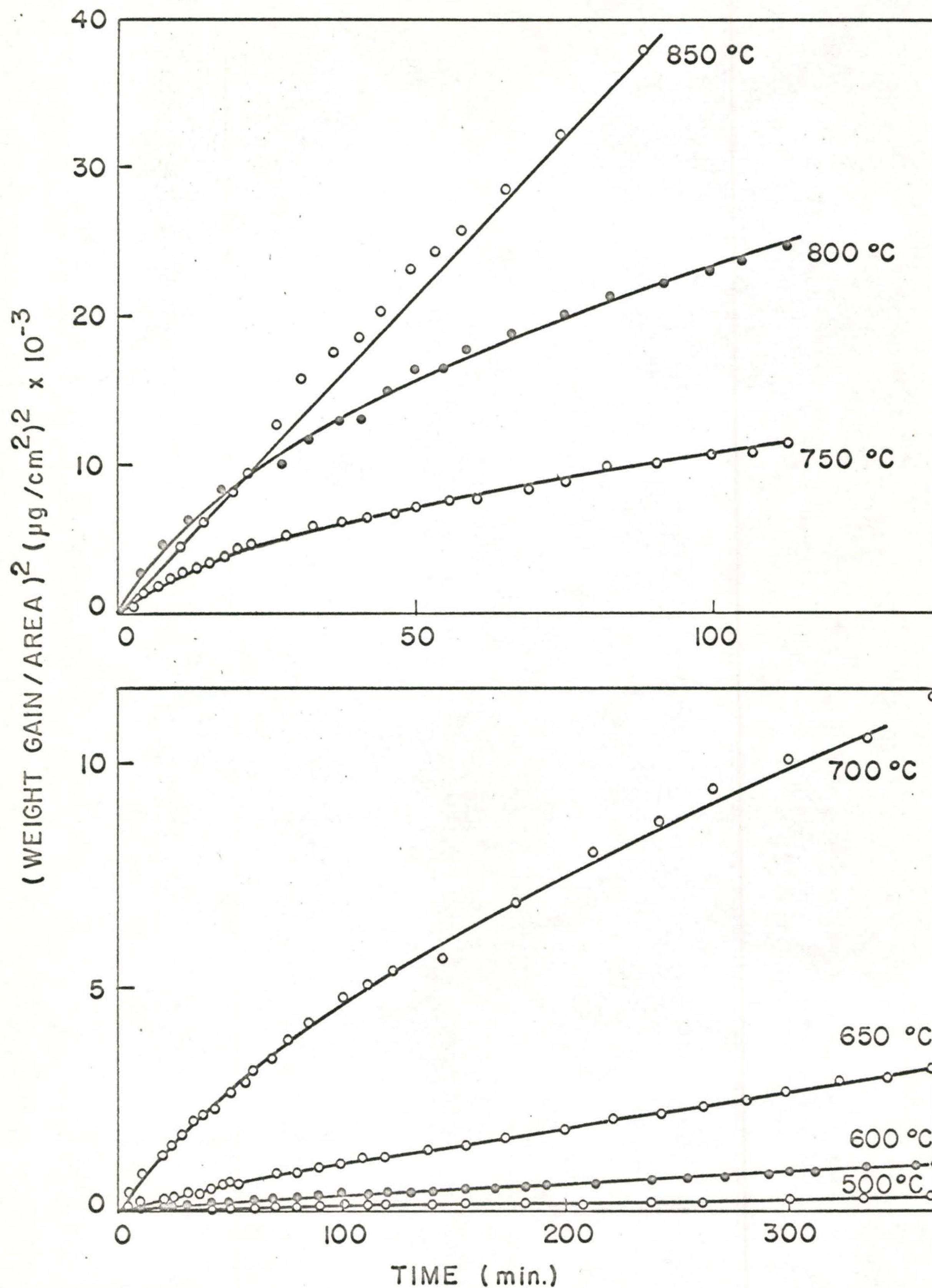

Figure 2: Oxidation kinetics for nickel in the temperature range 550° to 850°C

K_p, $f^\circ\alpha$ and k are shown plotted versus 1/T in Figures 3 and 4. The value of 41.7 Kcal/mole calculated from Figure 3 for the activation energy of the parabolic rate constant is in good agreement with the values of 44.2 and 45.9 Kcal/mole reported for the activation energy of nickel self-diffusion in polycrystalline and single crystal nickel oxide[45].

Evidence is now advanced to show that short-circuit diffusion plays a significant role in the rapid oxidation of nickel before the onset of parabolic oxidation. If the initial fraction of nickel sites within low resistance paths in the oxide film, f°, is independent of temperature,

$$f^\circ\alpha = f^\circ D_B/D_L = f^\circ \frac{D_B^\circ}{D_L^\circ} \exp\ (E_L - E_B)/RT \tag{24}$$

The activation energy, $E_L - E_B$, calculated from the least square plot of Figure 4 is 6.2 Kcal/mole. Accordingly, the ratio of E_B/E_L of 0.86 lies in the upper limit range reported for the activation energies of short-circuit and lattice diffusion[60,61]. Moreover, an estimate may be made of the initial fraction of sites from the values of the pre-exponential factor, $f^\circ D_B^\circ/D_L^\circ$, calculated from the plots in Figure 4. Employing the approximation D_B°/D_L° is equal to unity[60,61], $f^\circ \sim 7.5 \times 10^{-2}$ for nickel oxide. The short-circuit paths may then be associated with 10Å diameter dislocation pipes at an approximate density of $10^{11}/cm^2$. This represents very defective material and short-circuit diffusion would be expected to play a prominent role in the rapid initial rates.

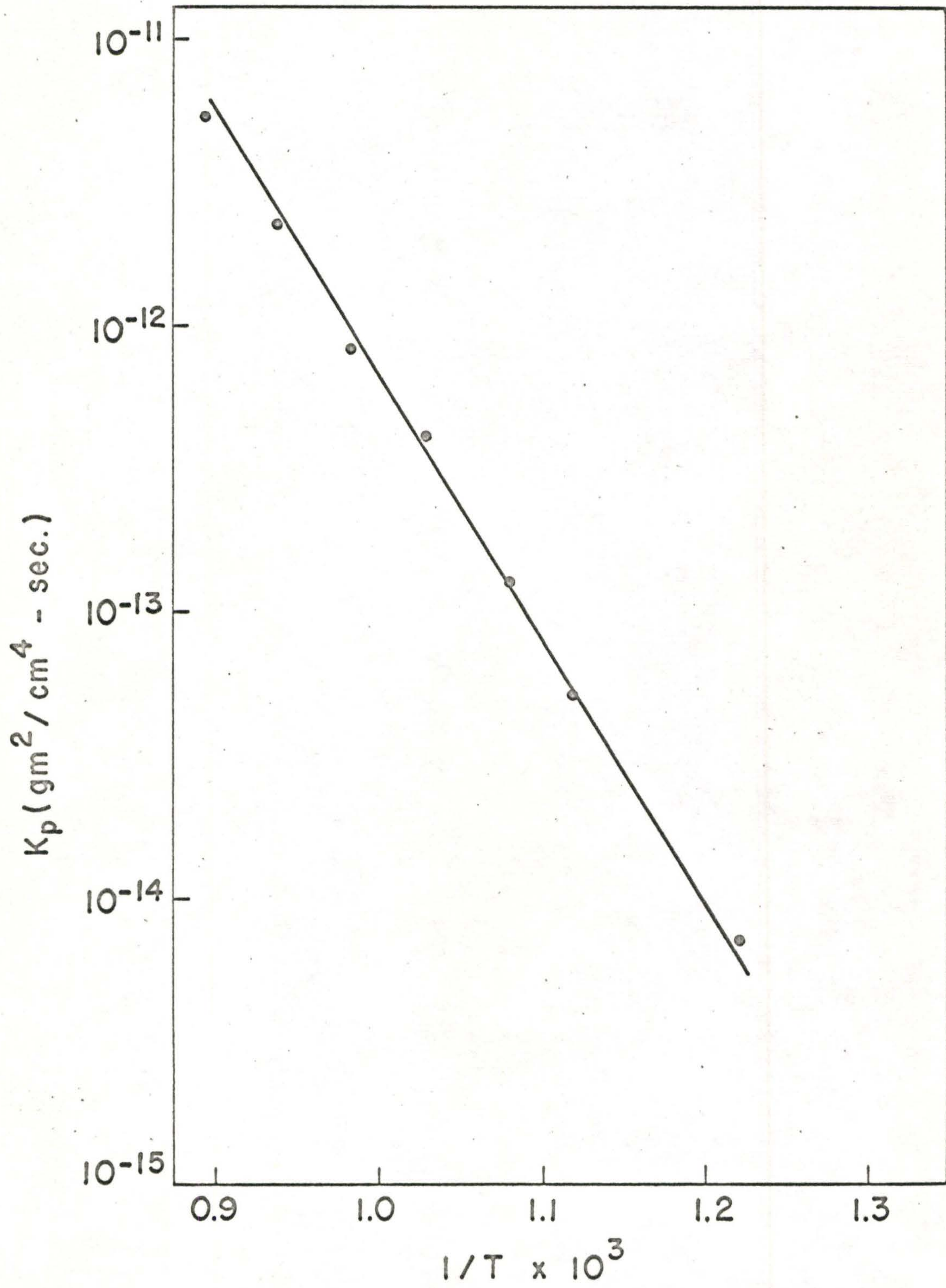

Figure 3: Parabolic rate constant for nickel versus reciprocal temperature

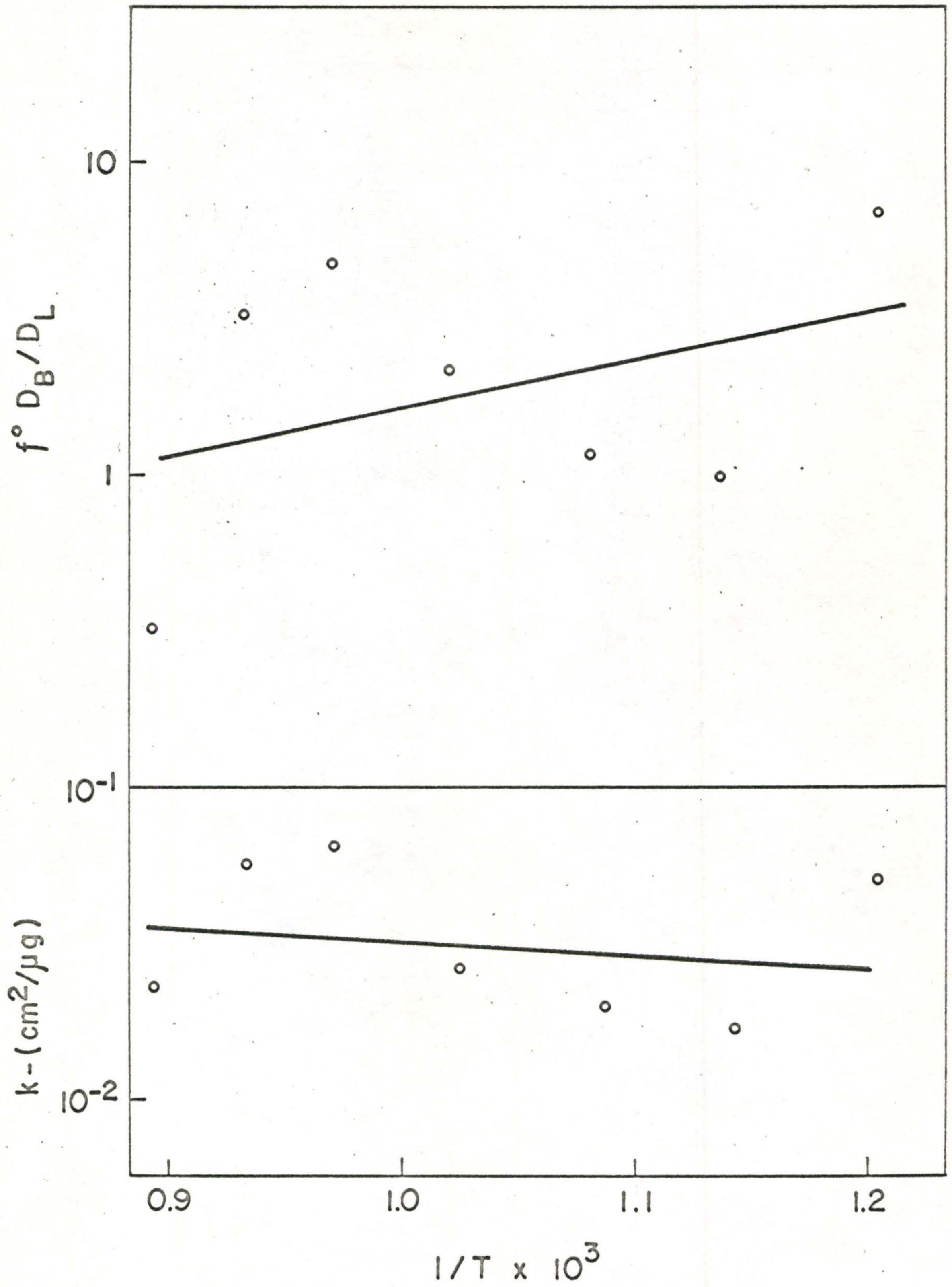

Figure 4: Log f°α and log k versus 1/T for nickel

3.3 Assessment of the Film Model

The application of the above model to the growth of thin oxide films on nickel suggests that short-circuit diffusion of nickel plays an effective role in the oxidation mechanism. It was assumed, however, that the short-circuit diffusion paths were simply random arrays of dislocations whose density decreased according to a first order rate equation. Transmission electron microscopy of oxide films less than 500Å in thickness formed on nickel[19], has shown that these films are composed of numerous small discrete oxide particles or crystallites which increase in size with continued oxidation. This indicates that the short-circuit diffusions paths are the crystallite boundaries. The contribution of short-circuit diffusion to the overall reaction rate will depend, therefore, on the process or processes, such as recrystallization and grain growth, which govern the increase in crystallite size. Accordingly, additional information concerning crystallite growth is required before a more precise oxide film model can be advanced. It would appear reasonable to employ the techniques of electron microscopy in order to obtain such information.

CHAPTER IV

Experimental Apparatus and Procedure

4.1 Sample Material and Surface Preparation

The material used in this investigation was nickel sheet of 99.94 per cent purity which had been cold rolled to a thickness of 0.03". The chemical analysis of this material is given in Table I. Oxidation specimens 1 cm x 1 cm in size were cut on a precision shear and a suspension hole drilled in each specimen. The hole diameter was selected so that the surface area removed was equal to the area introduced.

Each specimen was mounted flat in bakelite and metallographically polished through 240, 320, 400 and 600 grit silicon carbide using water as a lubricant. This was followed by polishing on a selvyt cloth impregnated with 1 micron diamond abrasive using kerosene as the lubricant. The kerosene was removed with petroleum ether and the specimen given a final polishing on a syntron vibratory polisher using a slurry of 0.3 micron alumina in water. After washing with acetone the specimen was stored in a desiccator.

Prior to oxidation the specimens were measured with a metric micrometer to 0.01 millimeters for computing their surface areas. They were then annealed for 12 hours at 825°C in a vacuum of 5×10^{-6} torr, weighed to ± 2 micrograms on a microbalance, and placed in the oxidation apparatus.

4.2 Oxidation Apparatus

A schematic diagram of the oxidation apparatus is shown in

TABLE I

Spectrographic Analysis of Nickel Sheet (in ppm)

Co	Ta + W	Al	Fe	Si	Cu	Mg	Cu	Ag	Zn	Nb	Cd	Bi	H_2	O_2	N_2
260	100	45	25	23	8	6	2	<1	<50	<30	<20	<3	2	85	2

Figure 5. The vacuum system which was capable of achieving a vacuum of 5 x 10^{-6} torr, as measured by a McLeod gauge, consisted of an oil diffusion pump backed by a mechanical pump. Liquid nitrogen traps were suitably placed to prevent the back diffusion of pump oil and to collect any mercury vapour from the McLeod gauge.

The furnace, which could be lowered or raised from around the reaction tube, consisted of a heating element of nichrome wire wound around a mullite tube and covered with a layer of refractory paste. The mullite tube and heating element were encased in refractory brick; the outer shell was constructed from asbestos board. The temperature variation in the hot zone was 2°C over a distance of three inches. The temperature was controlled to $\pm$2°C by a chromel-alumel thermocouple and a Pyro-Vane temperature controller which activated a mercury relay in the power circuit. The control thermocouple and a measuring thermocouple were both placed at the center of the hot zone between the mullite tube and the reaction tube. It was determined that a temperature difference of 2°C existed between the position of the thermocouple and the inside of the reaction tube.

Extra dry oxygen with a purity of 99.6 per cent minimum, and a dew point of less than -70°C was used in all tests. This oxygen was further purified by passing it through reduced copper oxide heated to 200°C, magnesium perchlorate and ascarite to remove hydrogen, water vapour, and carbon dioxide, respectively.

The reaction tube was a 30 mm. quartz tube joined to a pyrex tube of the same diameter at a point six inches above the top of the furnace when in the raised position. The top of the reaction tube was

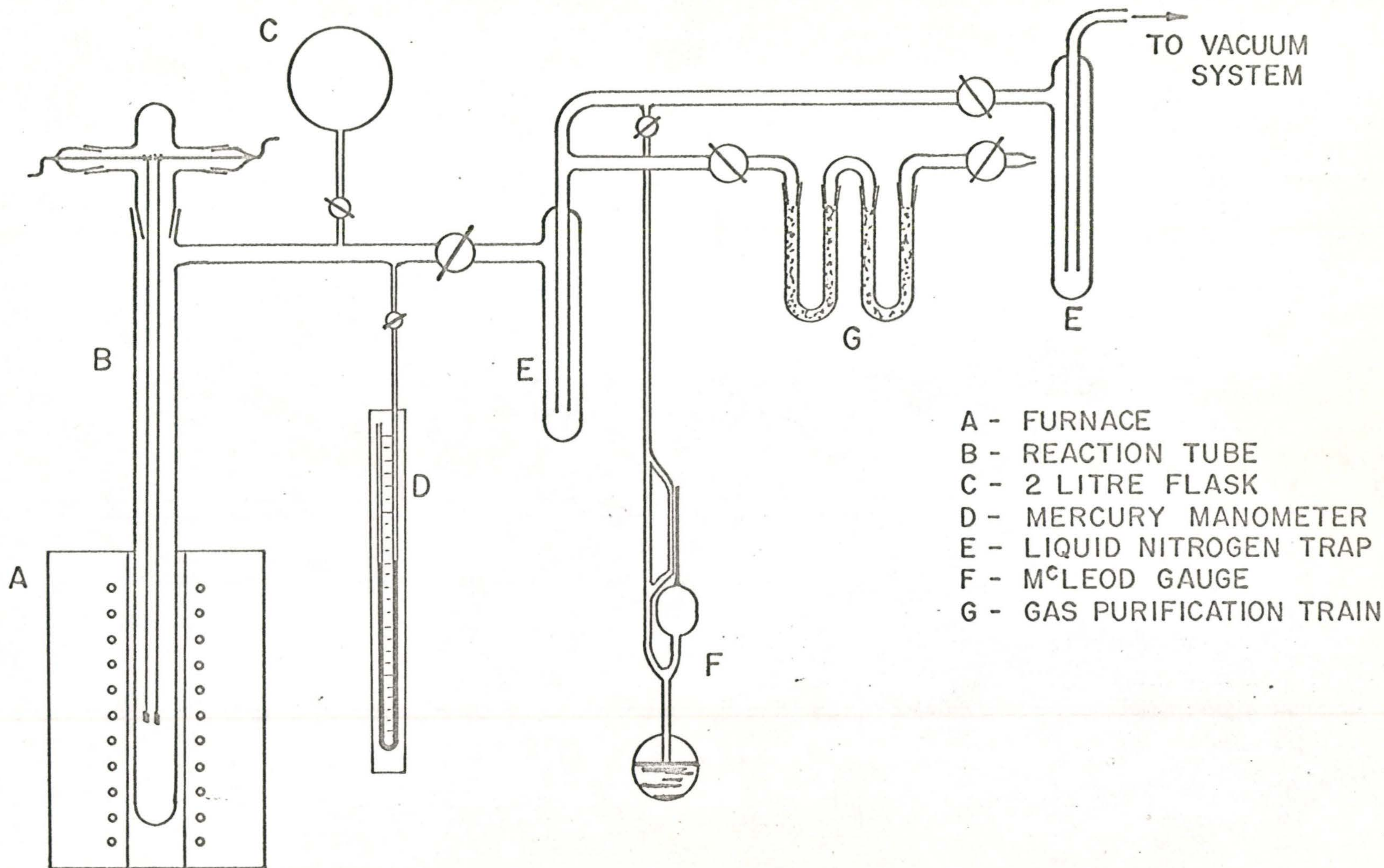

Figure 5: Schematic diagram of oxidation apparatus

fitted with a removable head which contained two glass winches. Samples to be oxidized were suspended by two 5 mil annealed platinum wires attached to the winches and they could be raised or lowered in the reaction tube by means of the winches.

The oxygen pressure in the reaction tube during oxidation tests was measured by a mercury manometer. Gold powder was placed in the glass tube connecting the manometer to the oxidation system so that any mercury vapour would form an amalgam with the gold and not reach the reaction tube. A two litre flask was also connected to the system close to the reaction tube to provide additional volume and prevent any significant changes in oxygen pressure from occurring during an oxidation test.

4.3 Oxidation Procedure

The oxidation apparatus was evacuated to 5×10^{-6} torr and the test samples were lowered into the reaction tube. The furnace was then raised up around the reaction tube so that the center of the hot zone corresponded to the position of the samples. The furnace which had previously been set to 30°C above the desired oxidation temperature was then reset to the proper temperature. This presetting of the furnace to a higher temperature compensated for the heat losses resulting when it was raised around the cold reaction tube. After approximately five minutes the temperature attained the desired value and oxygen was admitted to the reaction tube. After completion of an oxidation exposure the samples were raised to the top of the reaction tube and the furnace was lowered. The samples were removed from the reaction tube after cooling for 15 minutes and were weighed and stored in small vials

in a desiccator.

4.4 Stripping of the Oxide Films

Oxide film specimens required for electron microscopy were stripped from the metal surface by direct chemical attack of the underlying metal with a saturated solution of iodine in ethanol. Before stripping a sample, the oxide on its edges was ground off with silicon carbide paper, and the flat surfaces scored with a scalpel into 3 mm. squares. The oxide film specimens were washed several times in methanol following stripping in order to remove all traces of iodine. They were then stored in methanol.

For viewing in the electron microscope, film specimens were removed from the methanol by floating them on to electron microscope grids. These grids had previously been dipped into chloroform containing a few pieces of scotch tape. The adhesive from the tape was dissolved in the chloroform which on evaporating left sufficient adhesive on the grid bars to attach the oxide films. Care was taken to insure that adhesive did not cover the openings in the grids and interfere with the observations in the electron microscope.

4.5 Oxide Surface Replicas

Replicas of the outer oxide surface were obtained by a two stage replication technique. First, the sample to be replicated was covered with a layer of parllodion which was permitted to dry and then carefully removed. This relatively thick parllodion replica was placed in a vacuum evaporator and shadowed with gold-palladium. After shadowing, carbon was evaporated on the replica at normal incidence to form a layer 100 to 200Å thick. The parllodion-carbon composite was

then cut into small squares and placed on electron microscope grids with the parllodion in contact with the grids. The grids were then placed on a piece of filter paper soaked with amyl acetate which dissolved the parllodion leaving the desired shadowed carbon replica.

4.6 The Electron Microscope

The electron microscope used in this investigation was a Siemens Elmiskop I operated at 100 kV for transmission of oxide films and 60 kV for replicas. Bright and dark field electron microscope techniques were employed along with selected area electron diffraction[62].

CHAPTER V

Experimental Results

The experimental results are presented in the form of transmission electron micrographs, electron diffraction patterns, and graphs. The oxide film thicknesses quoted are average values calculated from weight gain data. In making these calculations, it was assumed that an oxide film of uniform thickness covered the entire metal specimen and that 1 $\mu g/cm^2$ of NiO was equivalent to 62.9Å[36].

5.1 Surface Preparation

It was desirable to select a method of surface preparation which would result in the formation of oxide films of relatively uniform thickness. For this reason, a number of methods, including chemical, electrochemical and mechanical polishing were investigated.

Transmission electron microscopy of stripped oxide films revealed that chemical and electrochemical polishing in various solutions, and coarse mechanical polishing (600 grit silicon carbide), resulted in oxide films of non-uniform thickness. Typical electron micrographs of oxide films grown on samples prepared by these methods are shown in Figures 6-9. This uneveness in film thickness appears to be related to irregularities in the metal surfaces, such as etch pits and steps or ledges for the chemical and electrochemical polished surfaces, and scratches in the case of coarse mechanical polished surfaces.

The method of surface preparation finally adopted is described in detail in the previous chapter. It involved fine mechanical polish ending with a slurry of 0.3 μ alumina in water. Smooth, scratch free

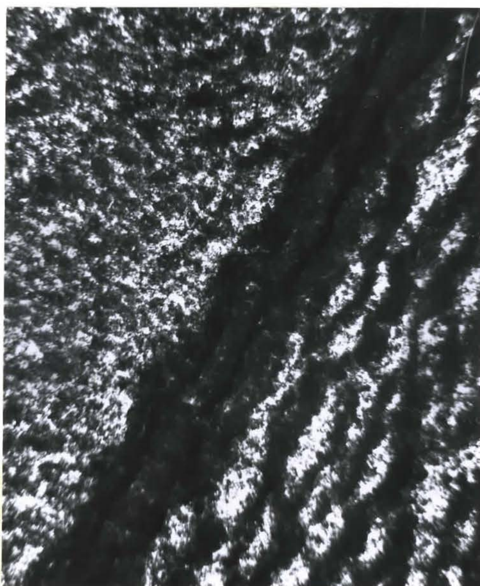

Fig. 6: A 1500Å NiO film formed at 500°C on a chemically polished metal surface. (4:1 nitric and water) x4000

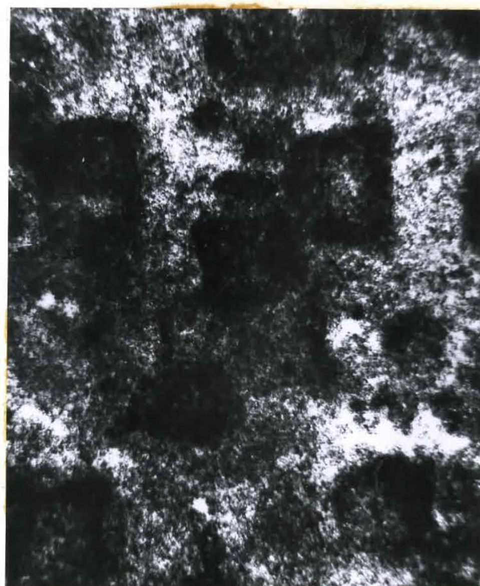

Fig. 7: A 2200Å NiO film formed at 500°C on a chemically polished metal surface. (4:1 nitric and methanol) x4000

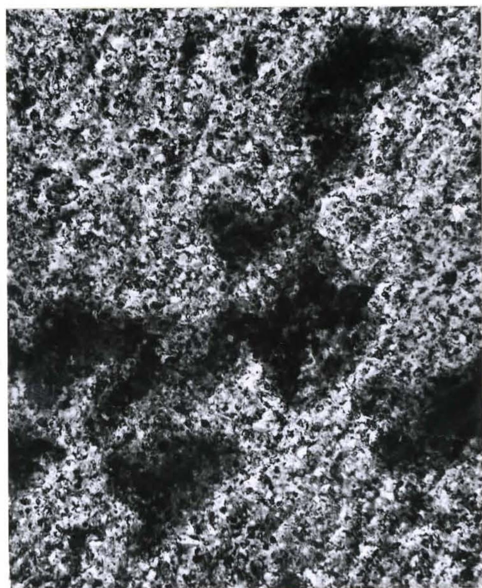

Fig. 8: A 1000Å NiO film formed at 500°C on an electrochemically polished metal surface (4:1 nitric and methanol) x20000

Fig. 9: A 1000Å NiO film formed at 500°C on a mechanically polished metal surface (600 grit silicon carbide) x20000

metal surfaces were produced by this method and the oxide films formed on individual metal grains were relatively uniform in thickness as seen in Figure 10.

5.2 Oxidation Kinetics

The oxidation kinetic curves for 500° and 600°C are shown plotted as weight gain per unit area versus time in Figure 11. The oxidation tests were carried out in pure oxygen with the weight gains being determined by weighing the specimens on a microbalance both before and after exposure. For the purpose of determining the reproducibility of these measurements, oxidation tests were carried out in triplicate for exposure times of 1 and 1.5 hours at 500°C and 1 hour at 600°C. The deviations from the mean values were ± 16, ± 27 and $\pm 20\%$ respectively. The maximum weight gains of 68 and 192 ug/cm^2 at 500° and 600°C corresponded to average film thicknesses of 4,300 and 12,000Å, assuming that 1 ug/cm^2 was equivalent to a film thickness of 62.9Å[36].

The form of the oxidation curves shown in Figure 11 are similar for both temperatures, exhibiting a continually decreasing rate of reaction with increasing film thickness. Such behaviour indicates that the reaction kinetics are controlled by the transport of reactants across the oxide film.

5.3 Transmission Electron Microscopy

5.3 (i) General Features

The transmission electron micrographs and inset electron diffraction patterns in Figures 12-15, illustrate the general features of thin nickel oxide films formed at 500° and 600°C. These films were composed of numerous small irregular shaped oxide crystallites. The films formed on different metal grains were different in both thickness

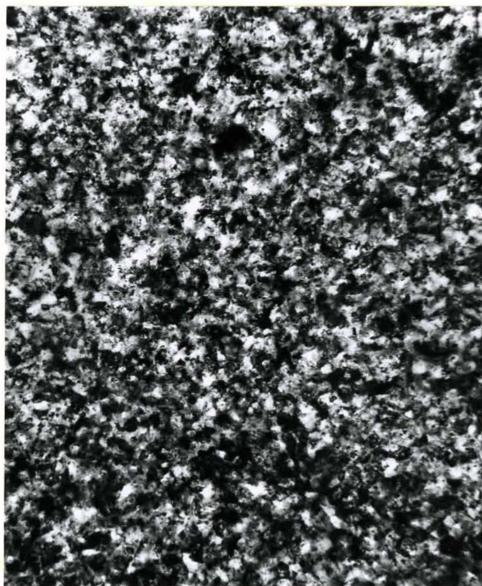

Fig. 10: A 700Å NiO film formed at 500°C on a mechanically polished surface (0.3 μ alumina) x20000

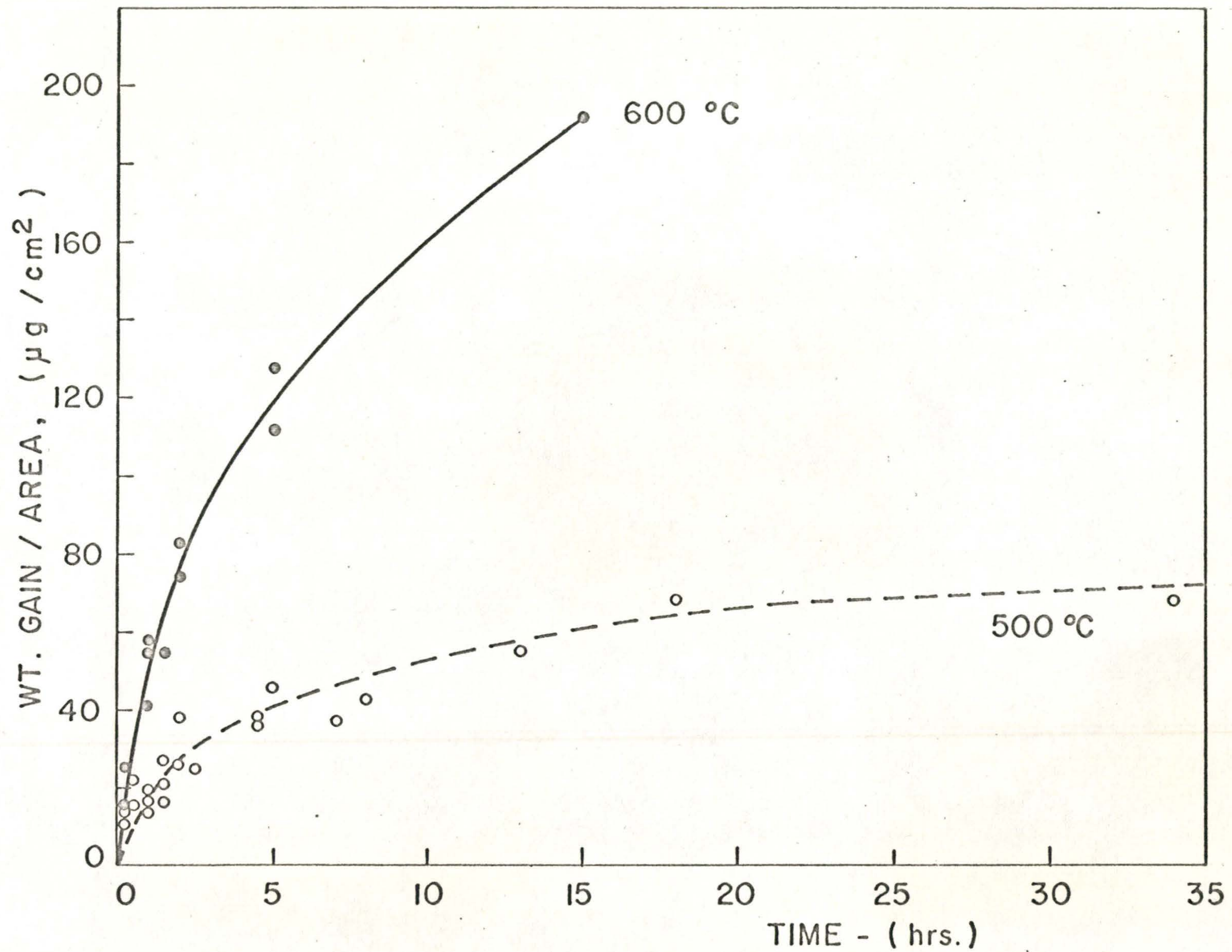

Figure 11: Oxidation kinetics for nickel at 500° and 600°C

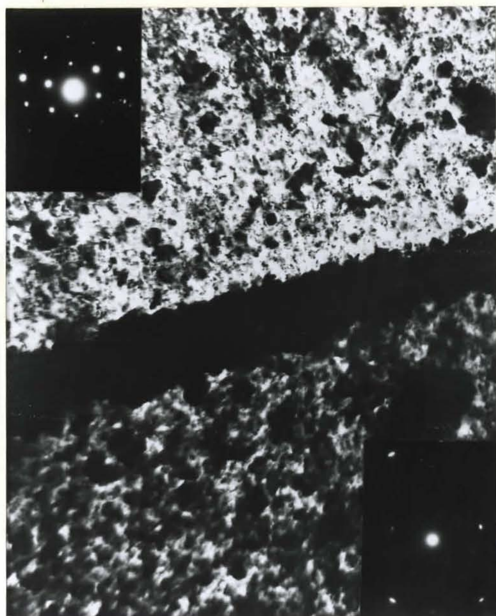

Fig. 12: A 1800Å NiO film formed at 500°C. x6000

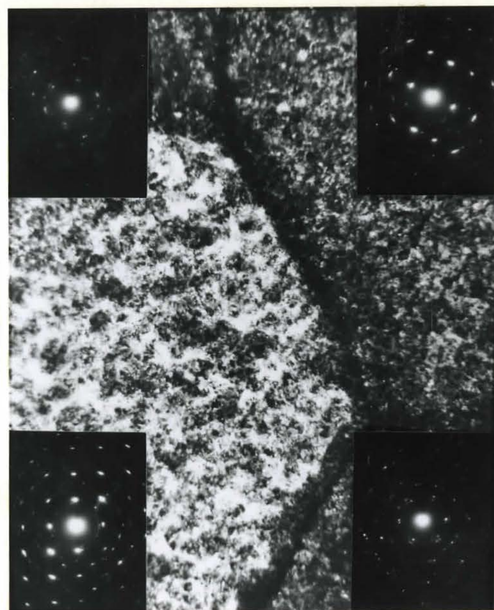

Fig. 13: A 1300Å NiO film formed at 600°C. x8000

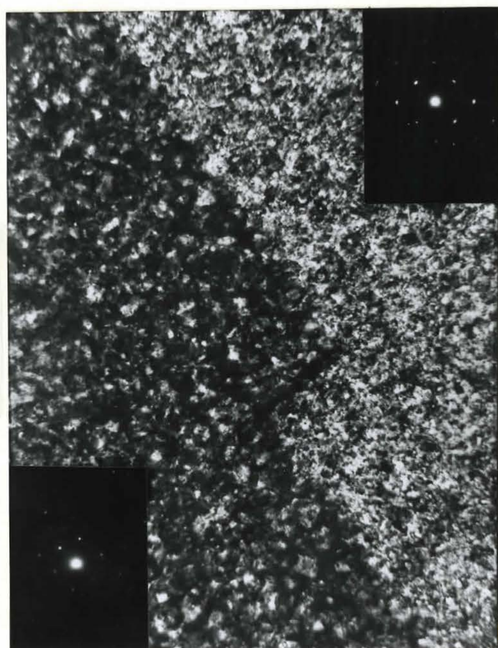

Fig. 14: A 1300Å NiO film formed at 600°C. x8000

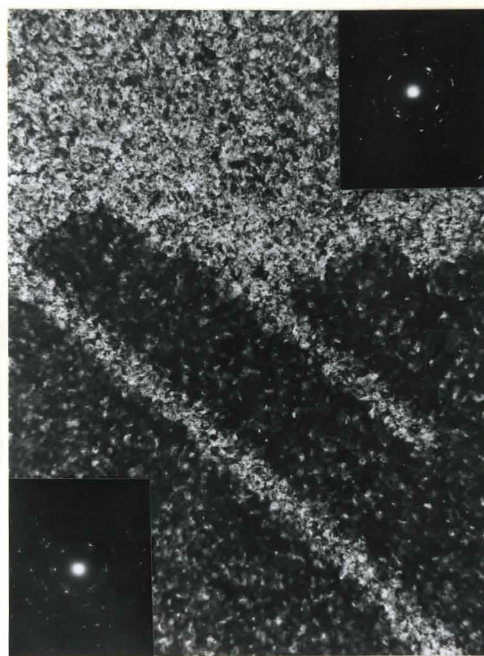

Fig. 15: A 700Å NiO film formed at 500°C. x8000

and orientation, and the electron diffraction patterns for the thinner or slower growing films more closely approximated single crystal spot patterns. In addition, varying degrees of localized thickening of the oxide occurred overlying the original metal grain boundaries, Figures 12 and 13, while no preferential oxidation was observed at twin boundaries, Figures 14 and 15.

As an oxide film thickened with increased oxidation time the average size of the crystallites increased. This is shown by the transmission electron micrographs in Figure 16. Furthermore, the electron diffraction patterns in Figure 16 indicate that as oxidation increased the misorientation of the crystallites decreased. With the exception of the film shown in Figure 16(a), which gave a polycrystalline diffraction pattern, all the films in Figure 16 were of a (110) orientation. For a given oxidation time films of the same orientation appeared to be of equal thickness. Therefore, the differences in film thickness shown in Figure 16 were due to increased oxidation and not orientation effects.

Replicas of the outer surfaces of oxide films of different average thicknesses, formed at 600°C, are shown in Figure 17. These replicas provide further evidence that the films were composed of crystallites which increased in size with continued oxidation.

5.3 (ii) Dark Field Electron Microscopy

In order that the crystallite sizes could be determined as accurately as possible the techniques of dark field electron microscopy were employed. In dark field microscopy only the crystallites contributing to a chosen diffracted beam were revealed thus making it easier to count and measure crystallites. To obtain a useful dark field micro-

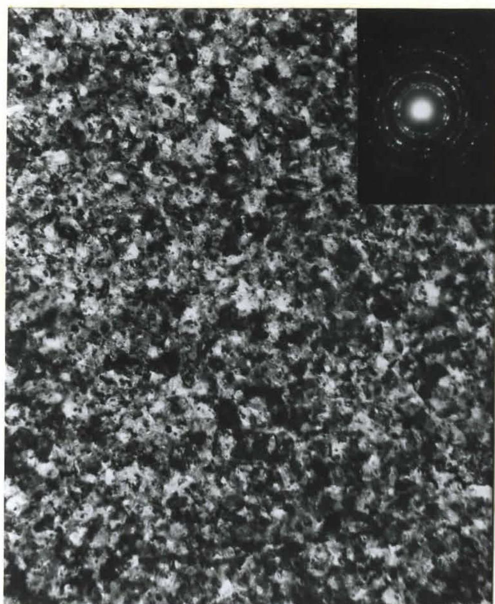

(a)

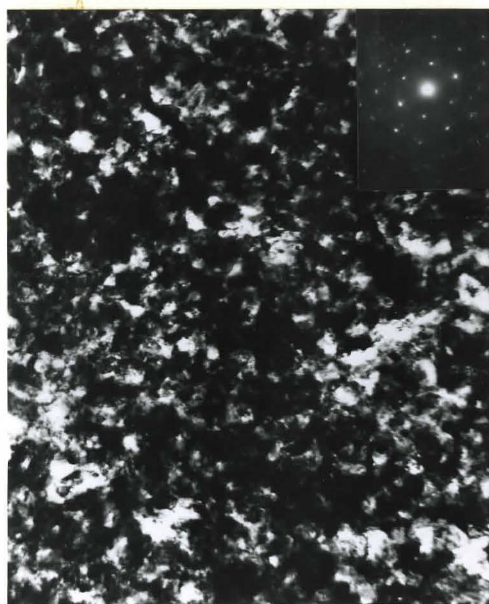

(b)

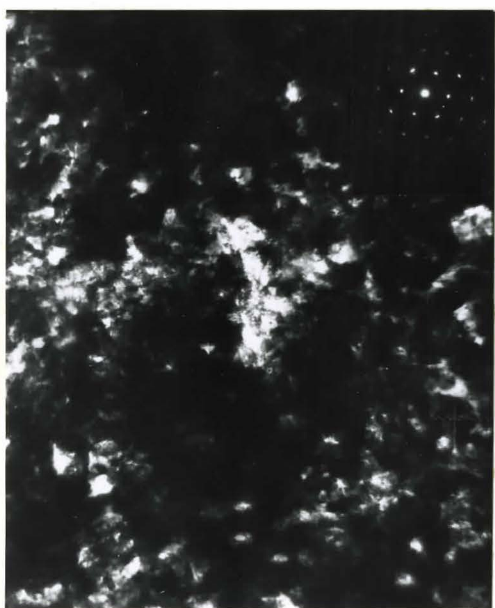

(c)

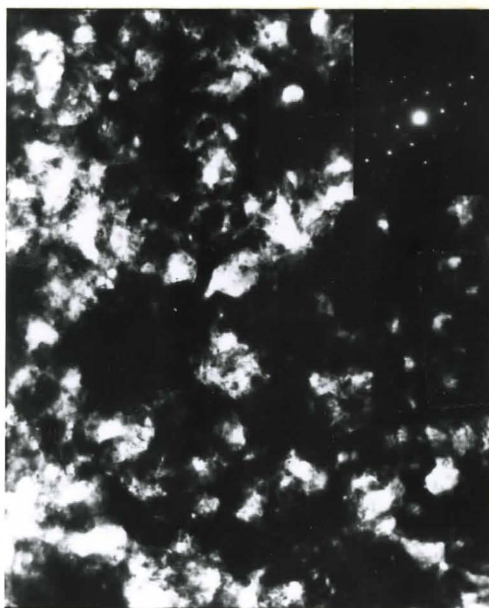

(d)

Fig. 16: NiO films formed at 500°C. (a) 700Å; (b) 1000Å; (c) 1900Å; (d) 2700Å. x2000

(a)

(b)

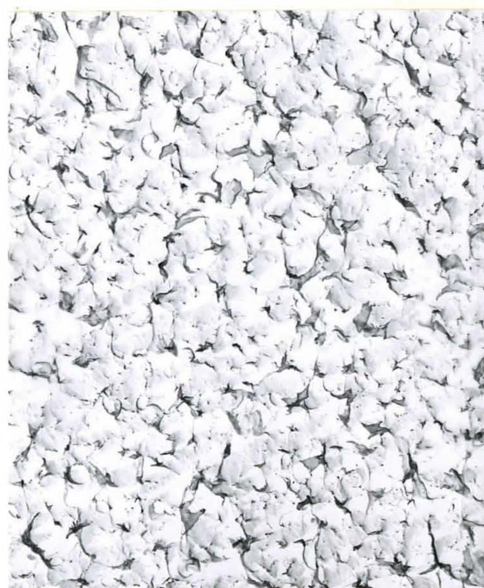

(c)

Fig. 17: Replicas of oxide films formed at 600°C. (a) 1300Å; (b) 2600Å; (c) 3500Å. x8000

graph the electron gun of the microscope was tilted so that a (111) diffracted beam became the central beam. This reduced the astigmatism and permitted accurate crystallite size measurements.

In Figures 18-21 the same oxide films are shown in both bright and dark field. It can clearly be seen that crystallite sizes can be more accurately determined from the dark field electron micrographs. The oxide films shown in Figures 18-21 were formed at 500°C and ranged in thickness from 700 to 1700Å. These figures indicate that over this thickness range there was little apparent change in the average crystallite size.

Figures 22-24 are a similar set of electron micrographs of oxide films formed at 600°C, ranging in thickness from 600 to 2600Å. While there is little apparent change in crystallite size for film thicknesses up to 1300Å, a marked increase in average crystallite size occurred as the film thickness increased from 1300 to 2600Å. In addition, Figure 24 shows that the average crystallite size for films greater than 2600Å in thickness could be determined just as accurately from bright field micrographs.

5.4 Crystallite Size Distribution

The distribution of sizes exhibited by the crystallites in each oxide film was determined from four dark field electron micrographs of the film enlarged to 80,000 times. In most cases one hundred crystallites, chosen at random in each enlargement, were measured to an accuracy of 0.5 mm., which corresponded to 125Å. For films greater than 2000Å in thickness the number of crystallites available for measuring was less due to their increased size. Therefore, only twenty-five

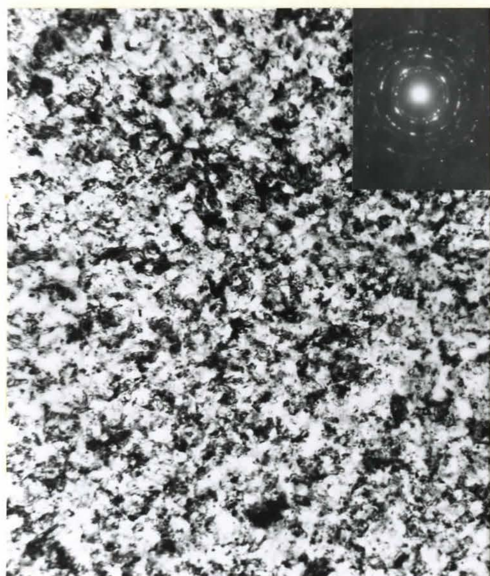

(a)

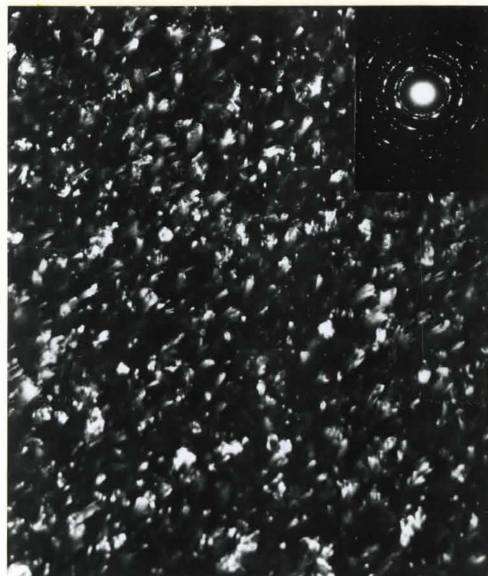

(b)

Fig. 18: A 700Å NiO film formed at 500°C. (a) bright field; (b) dark field. x20000

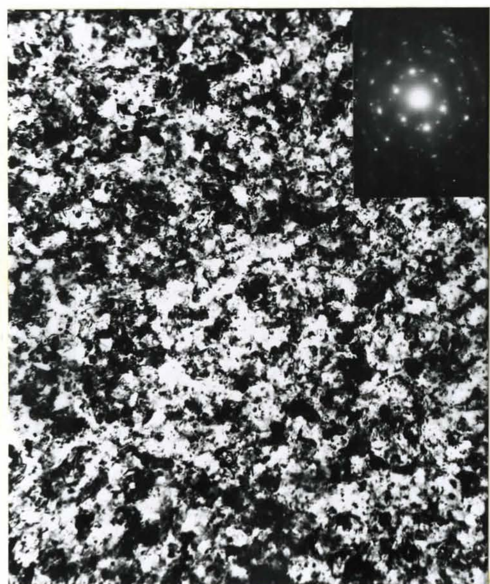

(a)

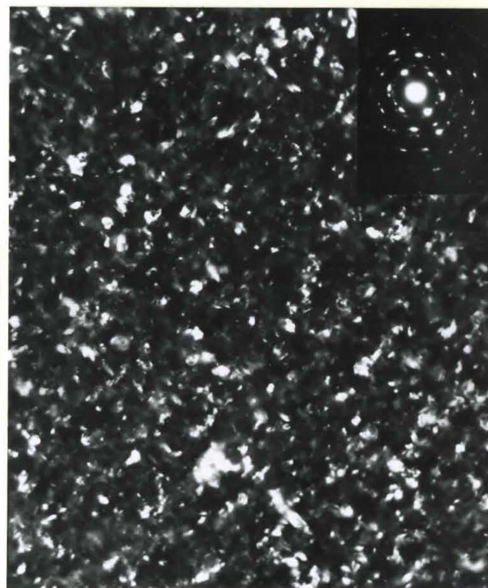

(b)

Fig. 19: A 1000Å NiO film formed at 500°C. (a) bright field; (b) dark field. x20000

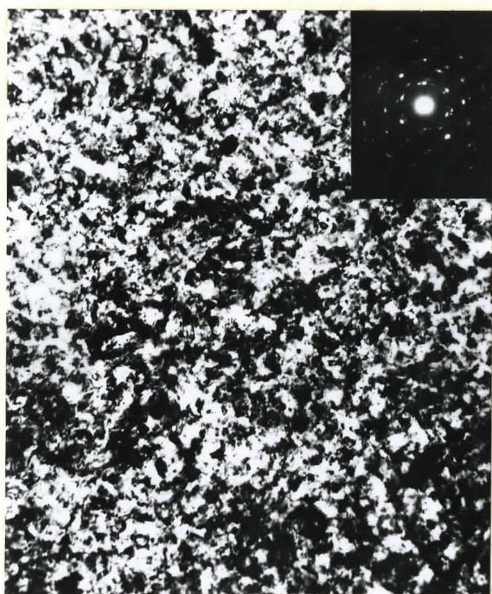

(a)

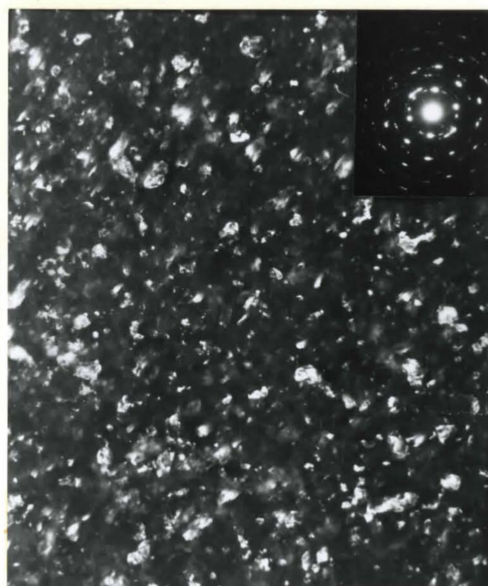

(b)

Fig. 20: A 1300Å NiO film formed at 500°C. (a) bright field; (b) dark field. x20000

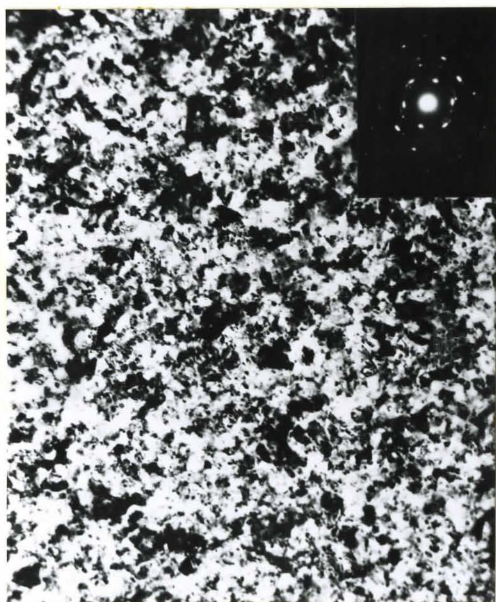

(a)

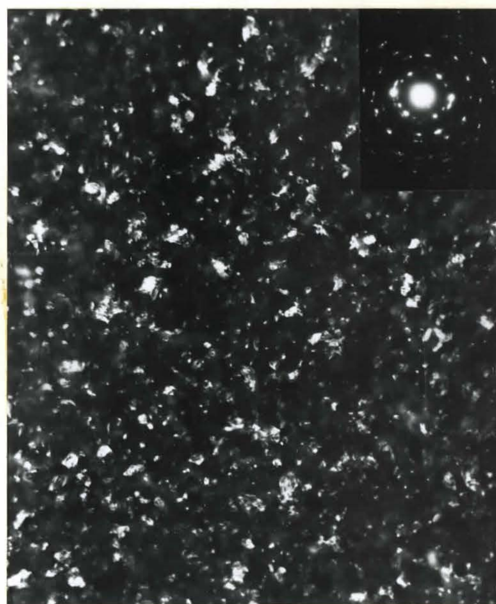

(b)

Fig. 21: A 1700Å NiO film formed at 500°C. (a) bright field; (b) dark field. x20000

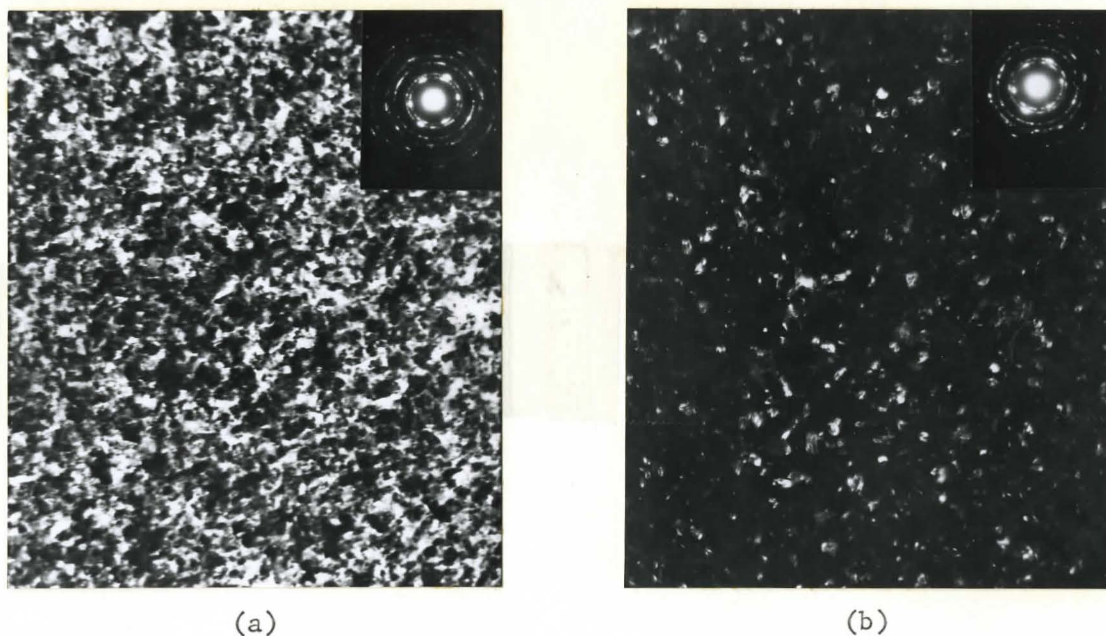

(a) (b)

Fig. 22: A 600Å NiO film formed at 600°C. (a) bright field; (b) dark field. x20000

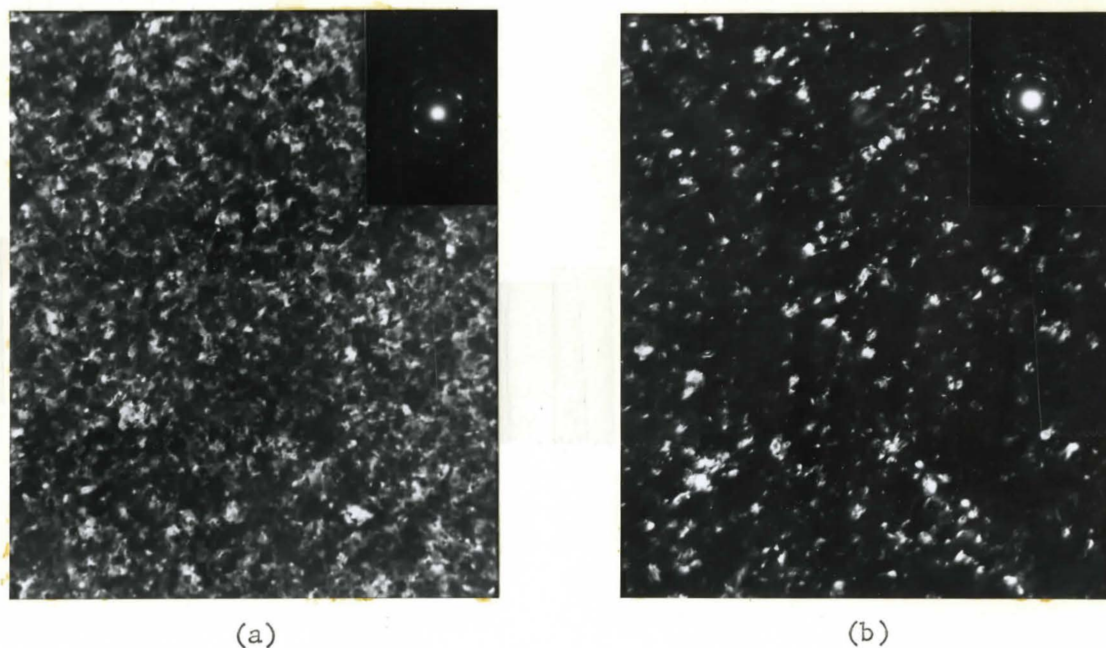

(a) (b)

Fig. 23: A 1300Å NiO film formed at 600°C. (a) bright field; (b) dark field. x20000

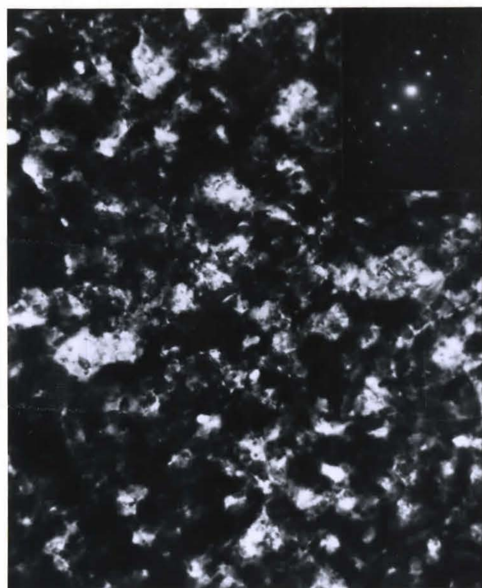

(a)

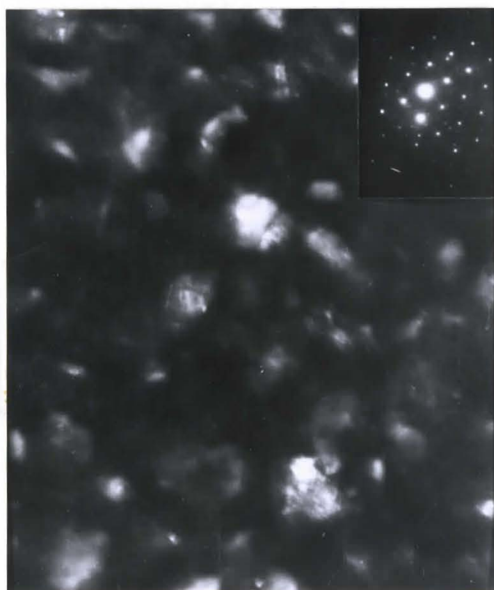

(b)

Fig. 24: A 2600Å NiO film formed at 600°C.
(a) bright field; (b) dark field. x20000

crystallites could be measured in each enlarged micrograph. In all cases, however, the number of crystallites measured was considered to be large enough to yield a good approximation to the true distribution.

The crystallite size distribution for a number of oxide films formed at 500° and 600°C are shown plotted as fraction of crystallites versus crystallite size in Figures 25 and 26. In Figures 27 and 28 the average crystallite size is shown plotted as a function of time and oxide film thickness, respectively. Figure 27 shows that at both 500° and 600°C the average crystallite size increased rapidly after having remained constant at approximately 100 to 150Å for an initial period of time. This sudden increase occurred sooner and the subsequent rate of growth was greater at the higher temperature. Figure 28 shows that at both 500° and 600°C this sudden increase in crystallite size did not occur until the films had reached thicknesses in the order of 2000Å.

While all of the above data was obtained from (110) oriented films, the (100), (111) and (112) orientations were also checked. The above results proved to be consistent for all these orientations.

5.5 Dislocation Structures

Nearly all of the films examined in this investigation were composed of oxide crystallites, with their boundaries being the only observable type of structural defect. There were, however, a number of films in which it was possible to distinguish dislocations. Figure 29 shows an oxide film which was taken from a specimen oxidized to an average thickness of 1800Å at 500°C. Dislocation tangles can be seen in the thinner areas of this relatively uneven film. The dislocation density in the thinner areas was $5 \times 10^{10}/cm^3$ as determined by random line

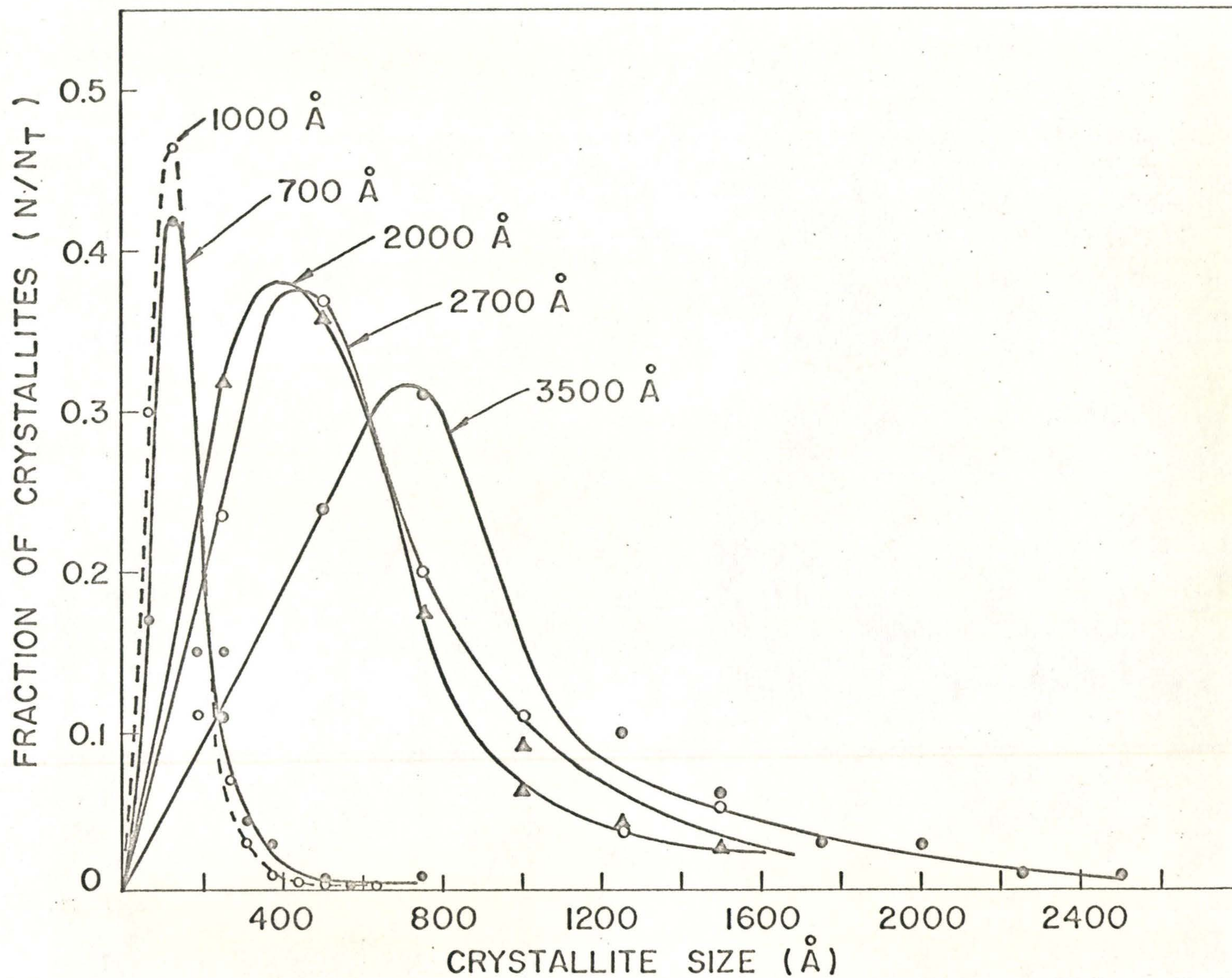

Figure 25: Crystallite size distribution for oxide films formed at 500°C

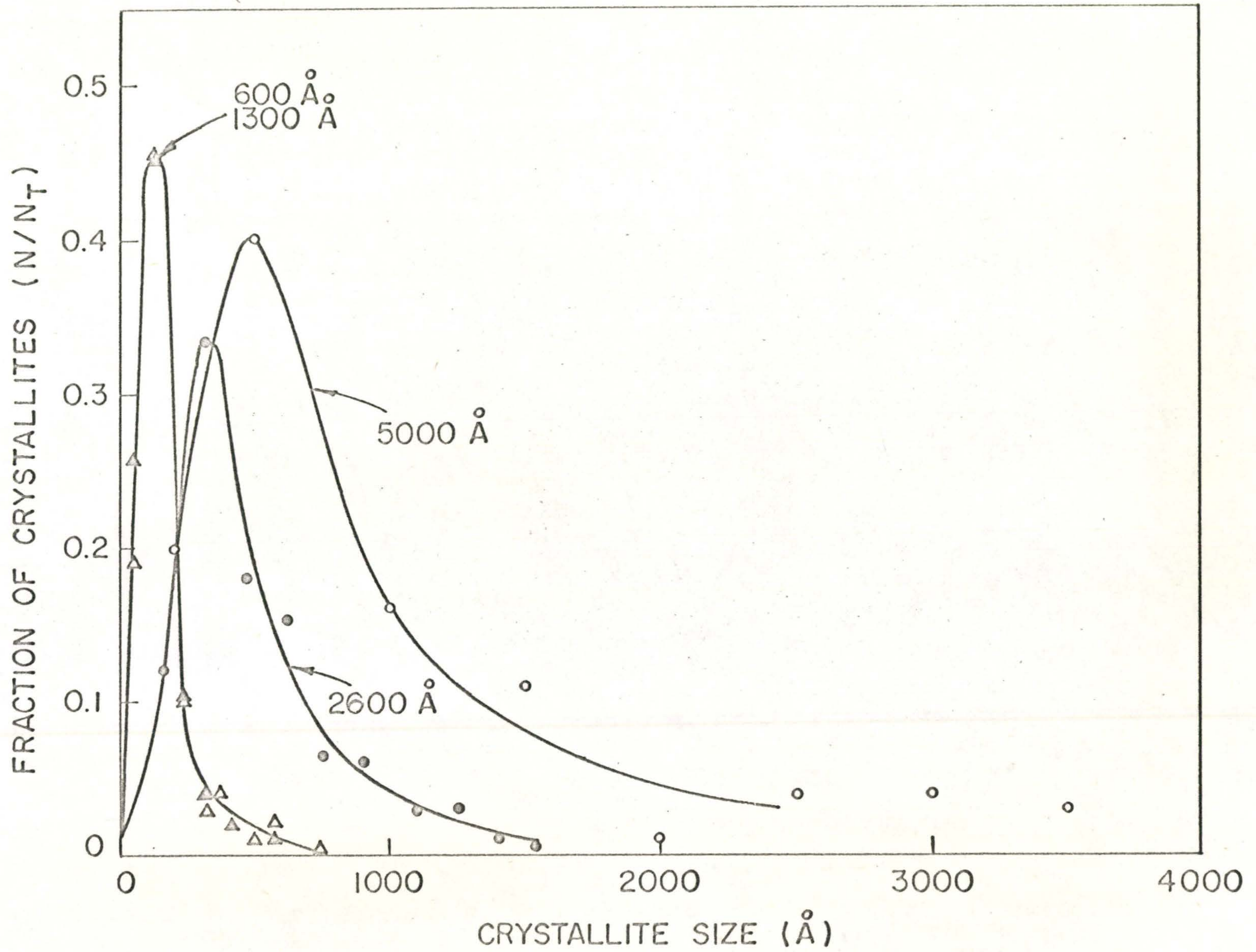

Figure 26: Crystallite size distribution for oxide films formed at 600°C

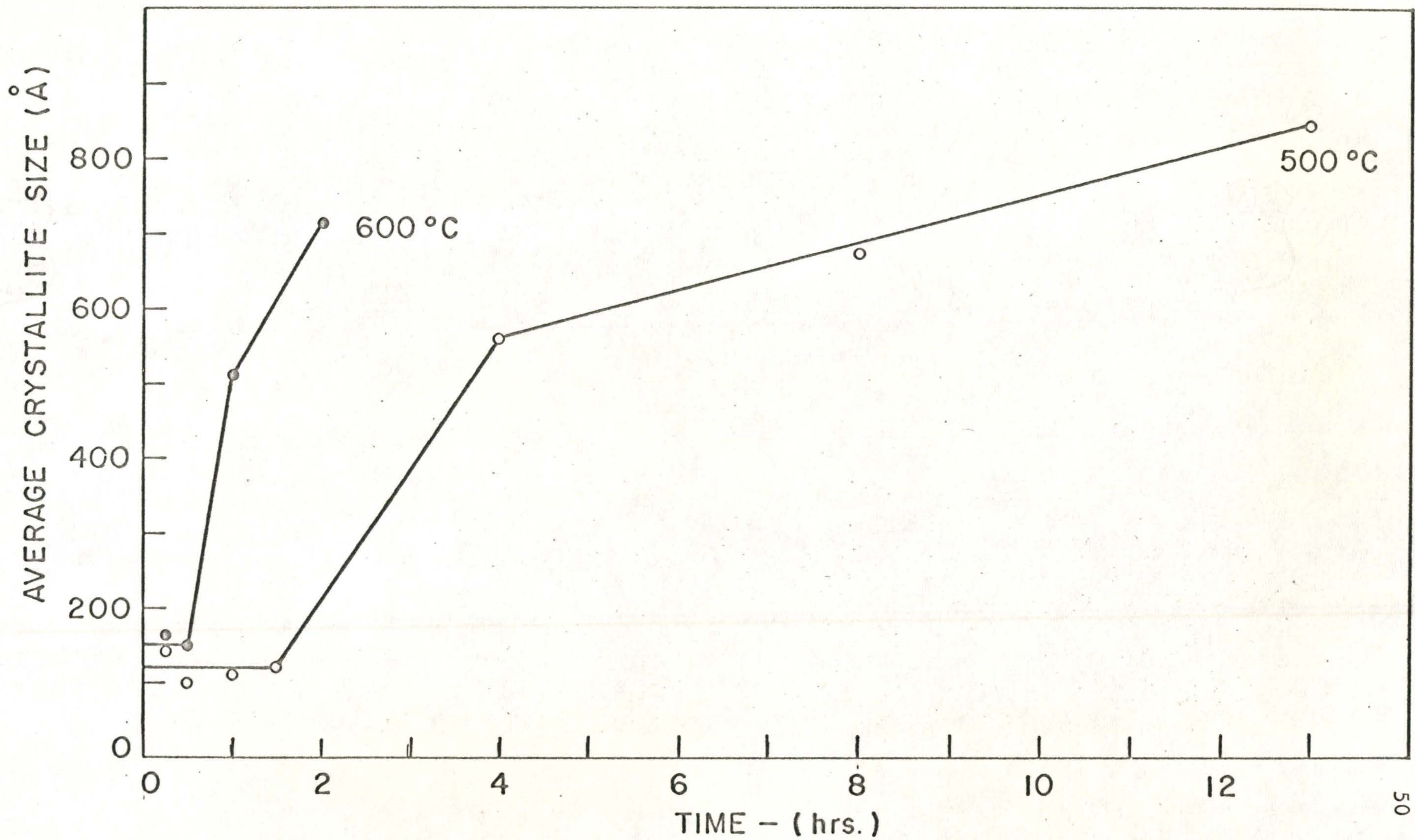

Figure 27: Average crystallite size versus oxidation time

MILLS MEMORIAL LIBRARY

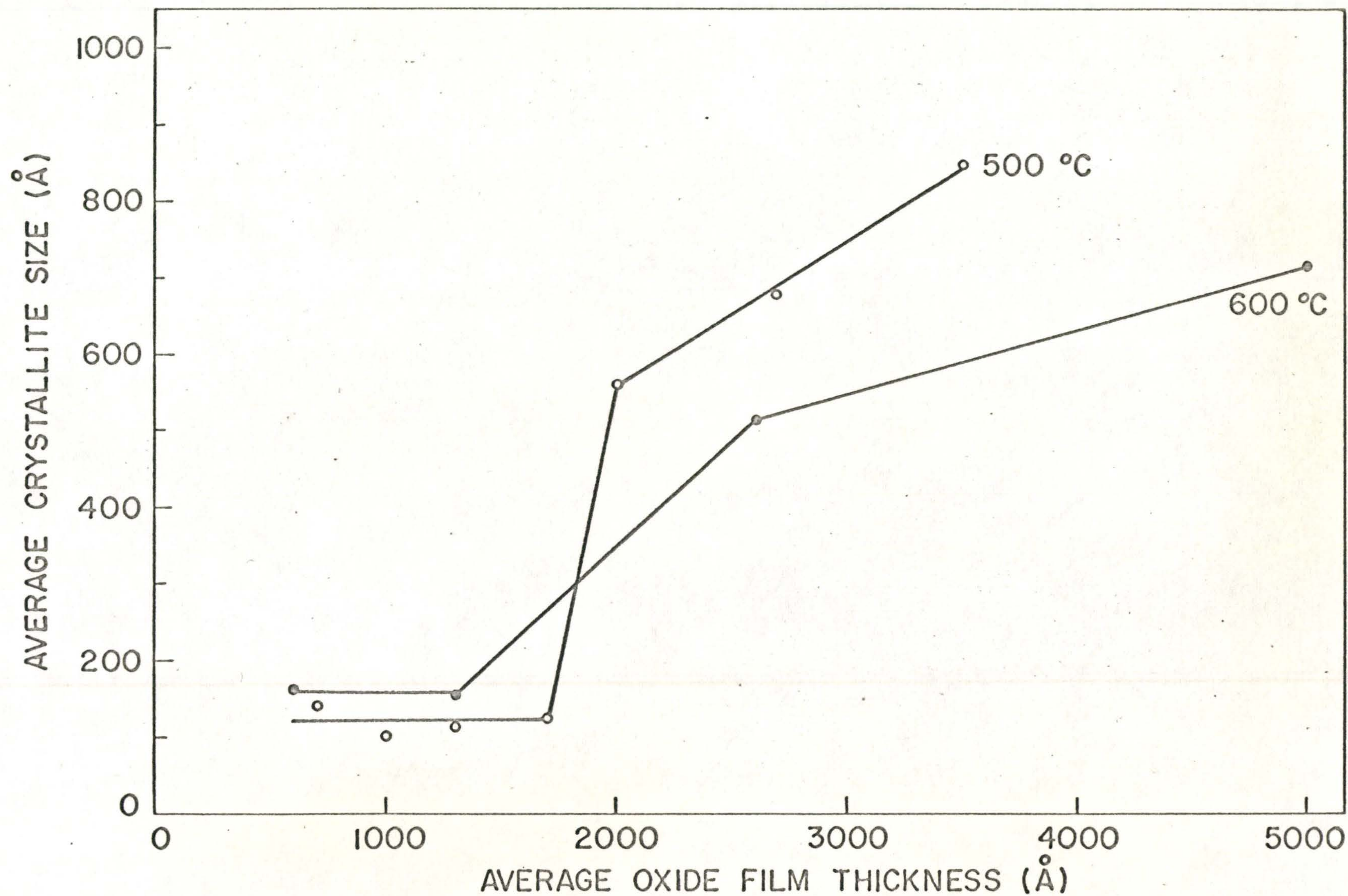

Figure 28: Average crystallite size versus average film thickness

counts assuming a thickness of 1000Å for these areas. Other films removed from the same specimen, an example of which is shown in Figure 12, exhibited the normal crystallite structure expected for films of this thickness. However, the orientation of the film shown in Figure 29 was (361), as indicated by its electron diffraction pattern, whereas all the other films examined showed low index orientations.

The absorption of electrons prevented the electron beam from penetrating films much greater than 3000Å average thickness. Oxide films of approximately 8000Å formed at 600°C, however, were extremely uneven in thickness and the electron beam was able to penetrate the thinner areas. A light transmission micrograph of such a film is shown in Figure 30 illustrating the variation in oxide film thickness from grain to grain as well as within individual grains. This latter feature can be more clearly seen by the electron micrograph in Figure 31. In addition, the proportion of a grain covered by the thicker oxide varied considerably and many grains were almost completely covered, Figure 32. Replicas of the outer surfaces of these extremely uneven films, Figure 33, showed that the thicker oxide regions extended outward from the surface.

At high magnifications, dislocation networks and sub-boundary walls were observed in the thin areas, Figure 34. The fact that the dislocations seen in Figure 34 are in good contrast indicates that they were lying almost parallel to the plane of the film. In a number of the thin areas it was not possible to bring dislocations into contrast and the film appeared to be divided into sub-grains with some thickening of the oxide in the neighbourhood of the sub-grain boundaries, Figure 35.

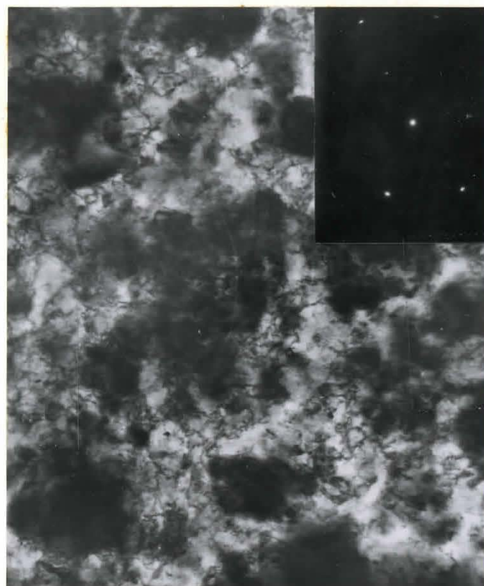

Fig. 29: An 1800Å NiO film formed at 500°C. x40000

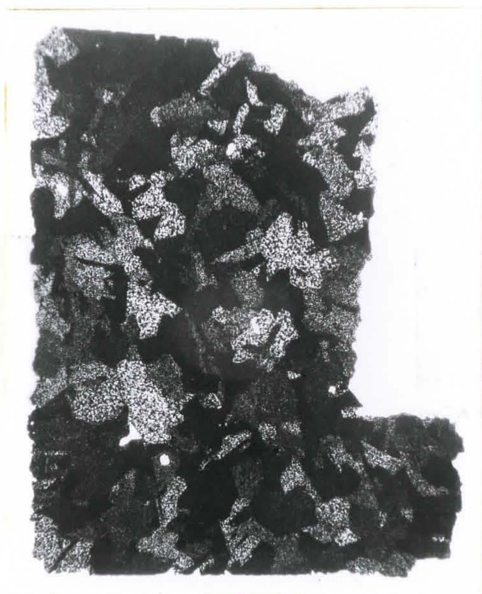

Fig. 30: A light transmission micrograph of an 8000Å NiO film formed at 600°C. x45

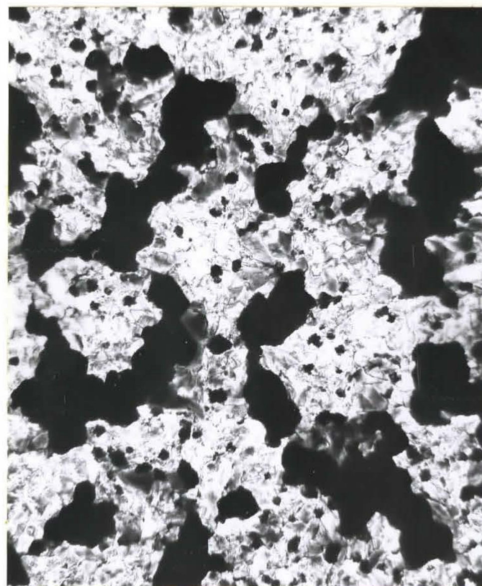

Fig. 31: An electron micrograph of an 8000Å NiO film formed at 600°C. x2000

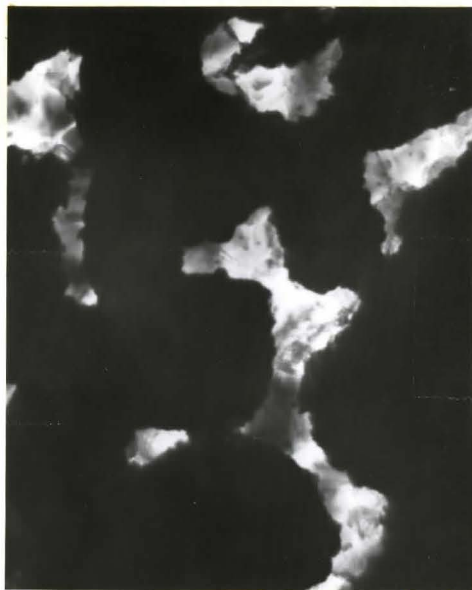

Fig. 32: An electron micrograph of an 8000Å NiO film formed at 600°C. x8000

Fig. 33: A replica of the surface of a 7000Å NiO film formed at 600°C. x8000

(a)

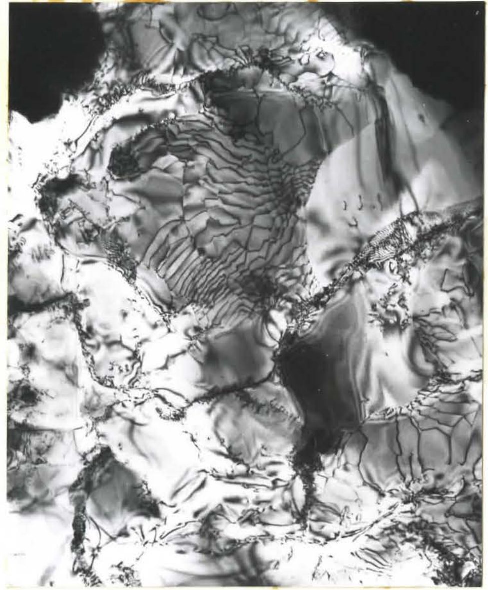

(b)

(c)

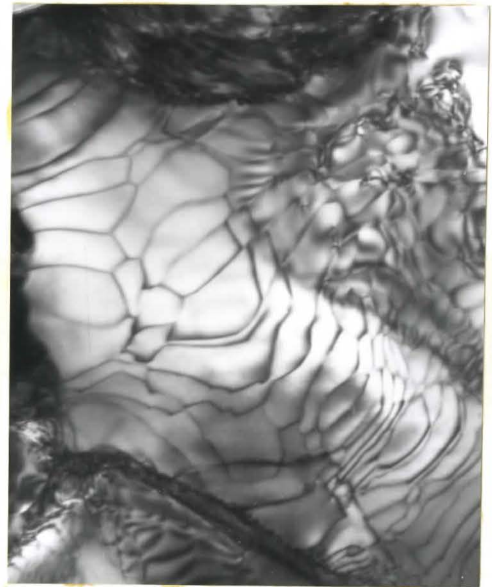

(d)

Fig. 34: Electron micrographs showing dislocation networks in the thin areas of an 8000Å NiO film formed at 600°C.
(a) and (b) x20000; (c) and (d) x60000

(a)

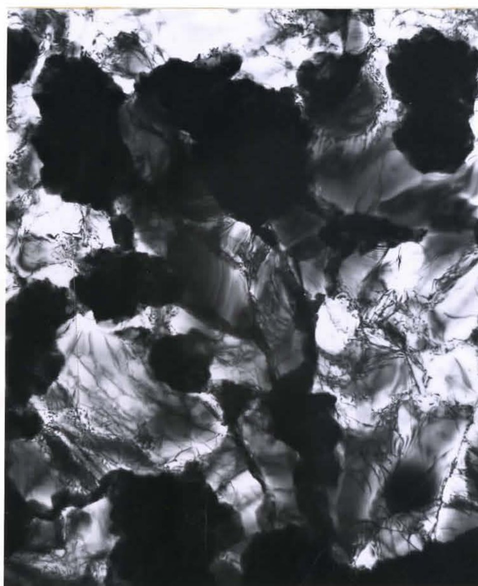

(b)

Fig. 35: Sub-boundaries in the thin areas of an 8000Å NiO film formed at 600°C. x12000

In these cases the dislocation networks were apparently perpendicular to the plane of the film.

The misorientation between adjacent sub-grains was determined by measuring the shift in the Kikuchi lines in the corresponding electron diffraction patterns. This method is capable of determining misorientations of 0.1°[63]. Figure 36 illustrates a case where the Kikuchi lines in the electron diffraction patterns from sub-grains A and B have shifted 3 mm. The Kikuchi lines, whose shift was measured, are shown by the extended dashed lines. This shift represents a misorientation of 20 minutes of arc as calculated from the relationship[64],

$$\Delta\theta = \frac{\lambda \Delta R}{\lambda L} \tag{25}$$

where $\Delta\theta$ is the angle of misorientation, λ is the wave length of the electrons at 100 kV, ΔR is the shift in Kikuchi lines on the original plates and λL is the electron microscope camera constant which was determined to be 2.1Å - cm[65]. By assuming the low angle tilt boundary approximation[66], this degree of misorientation represents a dislocation spacing of 550Å. This value is in excellent agreement with the dislocation space observed in Figure 34.

The above observations applied to most of the thin oxide areas examined. There were a few cases however, where the dislocations were more randomly distributed. Two examples of this are shown in Figure 37.

A few oxide films formed at 700° and 800°C were also examined during the course of this investigation. In all cases, these films were greater than 1000Å in thickness. They showed dislocation structures rather than oxide crystallites. Two electron micrographs are shown in

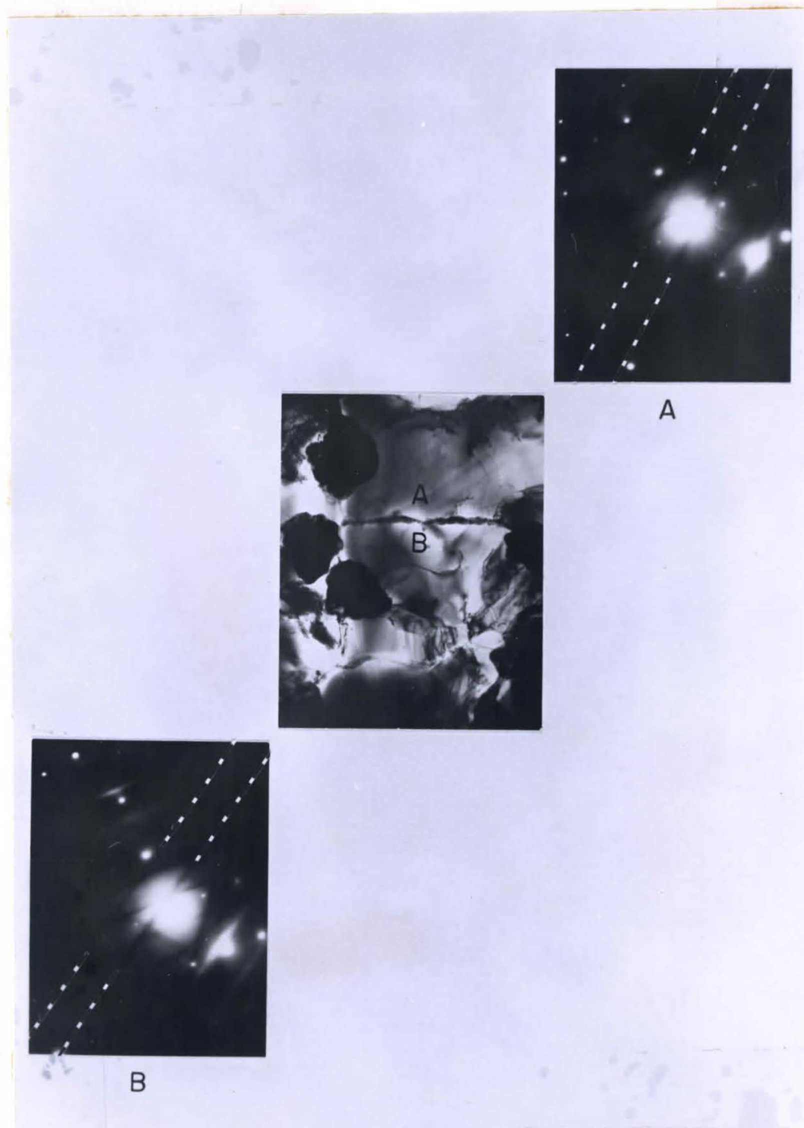

Fig. 36: An example of Kikuchi line shift.

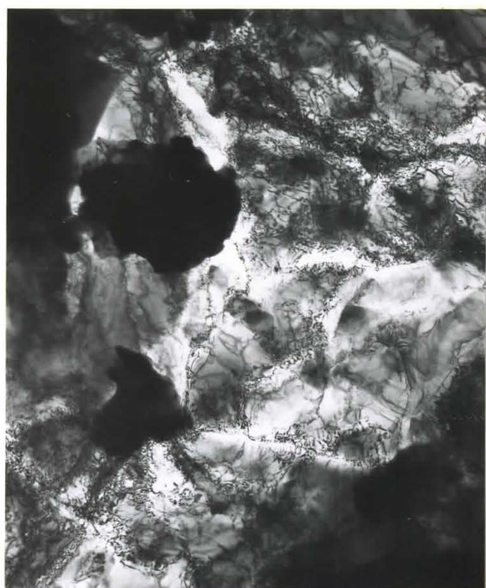

(a)

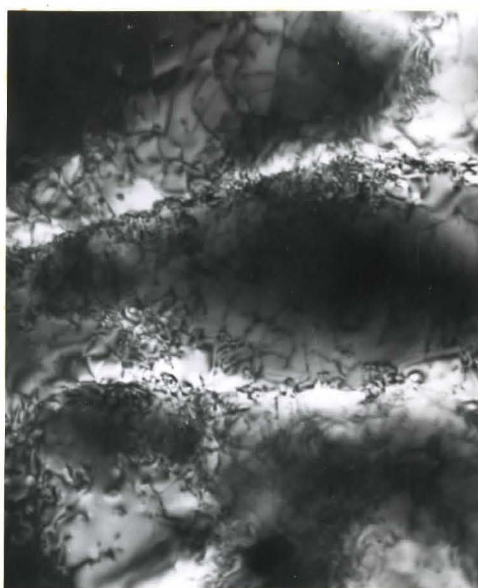

(b)

Fig. 37: Thin areas of an 8000Å NiO film formed at 600°C.
(a) x20000; (b) x60000.

(a)

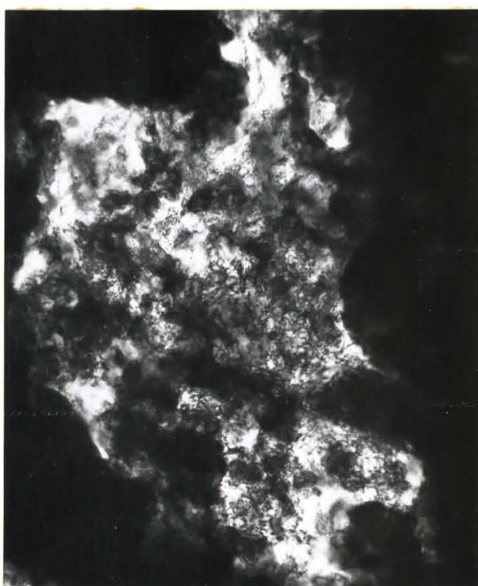

(b)

Fig. 38: NiO films formed at 800°C. (a) 1250Å average thickness; (b) 4700Å average thickness.

Figure 38 for films of 1250Å and 4700Å grown at 800°C. In Figure 38(a) it can be seen that this film was relatively uneven in thickness and the dislocations appeared to be forming cell walls in the thinner areas. The thicker oxide film, shown in Figure 38(b), was extremely uneven in thickness and a high density of randomly distributed dislocations was present in the thin areas. Since all these films were either of a (100), (110) or (111) orientation, the observations cannot be attributed to effects of high index orientations.

CHAPTER VI

Discussion

The types of structural defects present in thin nickel oxide films and the changes they undergo during the course of the oxidation reaction have been described in the previous chapter. In the following sections, these observations are correlated with short-circuit and lattice diffusion of nickel in the oxide films. This correlation leads to an understanding of the morphological development of the oxide films and to the development of an oxide film model for interpretation of the oxidation kinetics.

The first section presented is a discussion relating differences in film growth rates on different metal grains, preferential growth of oxide at metal grain boundaries, and growth of non-uniform oxide films, to the nature of the short-circuit diffusion paths. In the second section, the change in average crystallite size with oxidation time is described in terms of recrystallization and grain growth processes occurring in an oxide film. Finally, an oxide film model is advanced to correlate the oxidation kinetics with the observed film structures.

6.1 General Discussion

The nickel oxide films were relatively uniform in thickness on individual metal grains for thicknesses up to 3500Å at 500°C and 5000Å at 600°C. For a given average film thickness, the oxide crystallites of the film were approximately the same size on all metal grains, even though the film varied in thickness and orientation from one metal

grain to another, Figures 12-15. Therefore, the amount of boundary material available for short-circuit diffusion was the same for all grains. The electron diffraction patterns from the thinner areas in Figures 12-15, indicated that the misorientation between crystallites was less in these areas than in the thicker areas. It has been demonstrated for metals, that the effectiveness of a boundary to transport material by short-circuit diffusion decreases with decreasing misorientation for misorientations less than 28 degrees[31]. Thus, the contribution of short-circuit diffusion to the overall reaction rate would be expected to decrease with decreasing misorientation, resulting in a lower oxidation rate and a correspondingly thinner oxide film.

The orientation relationships between the oxide films and the nickel substrate were not determined in this investigation. Therefore, no conclusion can be made concerning the oxidation rate as a function of nickel orientation. It can be stated, however, that the growth rate of (110) oriented oxide was greater than the (100) orientation, Figures 13-15. Since only a few of the films examined contained the (111) and (112) orientations, it was not possible to determine their exact order of growth with respect to one another. However, they both appeared to grow at an intermediate rate between (110) and (100) oriented films. An example of a (112) oriented film is shown in the upper right hand corner of Figure 13.

The electron transmission micrographs in Figures 12 and 13 illustrate that preferential oxide growth has occurred at metal grain boundaries. This effect is to be expected on the basis that more rapid diffusion of material occurs at boundaries. As mentioned above, for

the case of oxide crystallites, the transport rate of reactants by a boundary depends on its misorientation. In a polycrystalline metal sample, the misorientation between grains would be expected to vary. Since the oxide film was obviously related in some manner to the metal substrate, the misorientation between oxide grains must also vary, resulting in different degrees of preferential oxidation at different grain boundaries, as can be seen by comparing Figures 12 and 13. The minimum amount of preferential oxidation, according to this argument, should occur at coherent boundaries, such as twin boundaries. In agreement with this reasoning, preferential oxidation was not observed at twin boundaries, Figures 14 and 15. Martius(54) observed a similar effect for the nucleation of nickel oxide on nickel. The size and number of nucleii formed on grain boundaries varied, while no nucleii were observed at twin boundaries.

All films which exhibited crystallites were relatively uniform in thickness within an individual metal grain. The plot showing crystallite size versus oxide film thickness, Figure 28, illustrates that the crystallite size was never greater than one-quarter of the film thickness. Accordingly, it would appear reasonable to treat the diffusion of nickel via crystallite boundaries as a random walk problem, as defined by Hart(32). Non-uniform film growth occurred only for those films which were no longer composed of crystallites. Instead, either dislocation tangles, Figure 29, or well defined dislocation networks, Figure 34, were observed in the films. The short-circuit diffusion paths, in these cases, were the dislocations and only those oriented normal to the metal surface contributed to the film growth.

Therefore, localized thickening of the film occurred in the neighbourhood of the more favourably oriented dislocations, resulting in the growth of non-uniform oxide films. This was especially true in cases where well defined dislocation networks existed in the film, Figure 35.

6.2 Recrystallization and Grain Growth

The curves shown in Figure 27, for the increase in average crystallite size with oxidation time for 500° and 600°C, are similar in form to those obtained for recrystallization and grain growth in metals[67], in which case per cent recrystallization is plotted as a function of annealing time. Furthermore, the effect of temperature was as expected for these processes. That is, the incubation time during which the crystallite size remained constant at between 100 and 150Å decreased, and rate of crystallite growth increased, for the higher temperature. It appears reasonable to conclude therefore, that the increase in crystallite size with oxidation time was determined by the processes of recrystallization and grain growth occurring in the oxide film.

The contribution of short-circuit diffusion to the overall reaction rate depends on the amount of boundary material present in the film. Accordingly, its role in the oxidation mechanism is determined by the recrystallization and grain growth of the oxide films.

During the incubation period, no change in the crystallite size distribution was detected but it is probable that some form of recovery process was active. As the oxide films thickened during this period their electron diffraction patterns more closely approximated single crystal spot patterns, Figures 18-21. Recovery may have occurred therefore, by internal rearrangements within the boundaries. Since no

quantitative data was obtained for the processes which occurred during the incubation period, only the changes in the distribution of crystallite boundaries are included in the subsequent treatment.

For grain growth in metals, Beck[68] has provided the relationship:

$$D_t^2 - D_o^2 = Kt \quad (26)$$

where D_o is the initial grain size, D_t is the grain size after some time t, and K is the growth constant. By assuming that grain growth occurs by a simple, thermally activated process, the grain growth constant K, can be represented by the Arrhenius relationship:

$$K = K_o e^{-Q/RT} \quad (27)$$

where Q is the activation energy for the process.

In Figure 39, $D_t^2 - D_o^2$ is shown plotted against t for the investigated temperatures of 500° and 600°C. Within the experimental certainty of determining the average crystallite sizes this equation gives excellent representation of the data. The values for the growth constant K at 500° and 600°C are equal to the slopes of the curves in Figure 39. Knowing these values and applying the Arrhenius relationship, equation (27), an activation energy of 19 Kcal/mole was calculated for the process controlling crystallite growth. This value is approximately equal to one-half the activation energy of 41 Kcal/mole reported for the lattice diffusion of nickel in nickel oxide[52]. Since grain growth has been considered to be controlled by boundary diffusion[69,70], for which the activation energy is of the order of one-half that for lattice

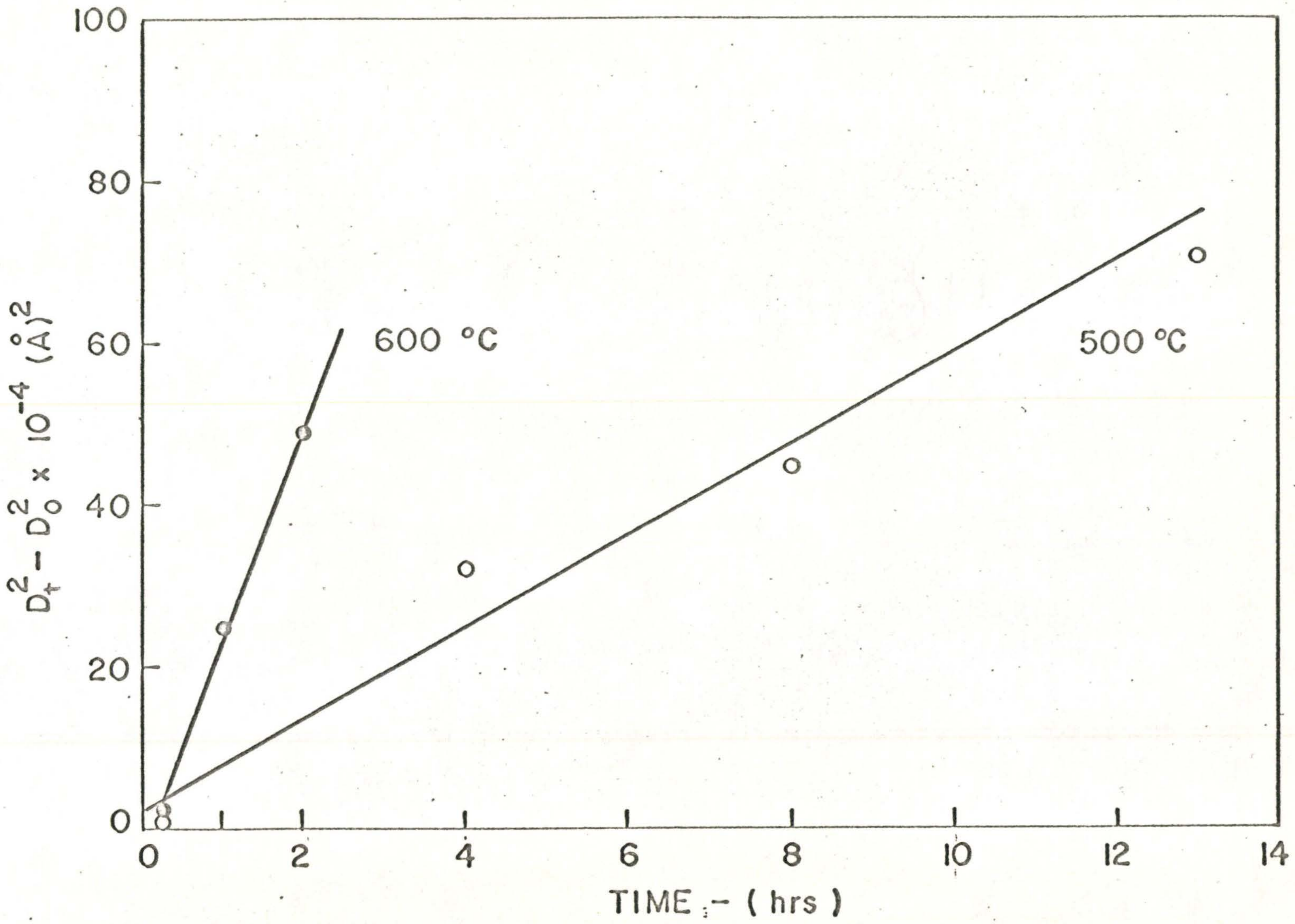

Figure 39: D_t-D_o versus oxidation time

diffusion[60], the calculated value of 19 Kcal/mole, while determined from data at only two temperatures, supports the previous conclusion that grain growth occurred in the films following recrystallization.

6.3 Correlation of Oxidation Kinetics with Film Structure

The crystallite dimensions in the initial oxide film, when film growth was relatively uniform, were always much less than the film thickness. For example, at 500°C the crystallite size was 100 to 150Å for films up to 1700Å in thickness and attained a maximum size of only 850Å for a film thickness of 3500Å, Figure 28. These results suggest that it would be appropriate to seek correlations of oxide film growth with short-circuit and lattice diffusion, according to the theory advanced by Hart[32]. A review of this theory involving short-circuit and lattice diffusion by a random walk process was presented in Chapter II.

In applying the Hart analysis for enhanced bulk diffusion in a crystal containing a large number of short-circuit diffusion paths, it is essential that the following requirement be met,[33]

$$2\ (D_L t)^{1/2} > l_d \tag{28}$$

where in the present case, D_L is the lattice diffusion coefficient of nickel in nickel oxide, t is the oxidation time, and the maximum distance for l_d is the crystallite size. The diffusion coefficients for nickel in nickel oxide at 500°C, obtained from Figure 1, lie within the range 1×10^{-15} to 2×10^{-18} cm^2/sec. For a one hour oxidation exposure at 500°C, the crystallites must be within the range 20 to 400Å. This approximation agrees reasonably well with the crystallite sizes found in this investigation. It would therefore appear appropriate to apply

the Hart analysis to develop specific refinements to the oxide film model discussed in the theoretical section. These refinements are based on the data obtained in this investigation for the processes of recrystallization and crystallite growth occurring in the oxide film.

6.3 (i) Oxide Film Model

An equation may be developed to describe the oxidation kinetics for nickel when oxidation leads to a uniform oxide film. In the light of the above considerations, identical assumptions for short-circuit and lattice diffusion are employed, as outlined in the theoretical considerations, Chapter III. The equation is formulated on the basis of Hart's analysis for diffusion in solids.

Accordingly, it is assumed that nickel migrates through the film by lattice diffusion and by diffusion within a random array of low resistance paths. These low resistance paths are associated with crystallite boundaries. The effective diffusion coefficient may be expressed as:

$$D_{eff} = D_L\ (1-f) + D_B f \qquad (29)$$

where D_{eff}, D_L and D_B are the effective, lattice and boundary diffusion coefficients respectively, and f is the fraction of total available nickel sites lying within low resistance diffusion paths. Under these conditions the driving force for oxidation is assumed to be the concentration gradient of nickel existing between the inner and outer oxide surfaces. The flux of nickel, according to Fick's first law of diffusion,[71] would be :

$$J_{Ni} = -D_{eff} \frac{dc}{dx} \tag{30}$$

where x is the film thickness. This concentration gradient for nickel would be relatively low and therefore may be assumed to be inversely proportional to film thickness. Thus,

$$\frac{dx}{dt} = \Omega J_{Ni} = \Omega D_{eff} \frac{\Delta c}{x} \tag{31}$$

where Ω is the volume of oxide per nickel ion.

The results of this investigation have shown that the fraction of surface area associated with boundaries was virtually constant during the initial stages of the reaction. In which case, the integration of equation (31) yields,

$$x^2 = 2 \Omega D_{eff} \Delta ct = Kp(eff)t \tag{32}$$

Thus, the initial reaction should be defined by a parabolic relationship in which the effective parabolic oxidation constant would contain terms for lattice diffusion, boundary diffusion and a constant fraction of sites within low resistance paths. This effective diffusion constant would be,

$$D_{eff} = D_L(1-f^\circ) + D_B f^\circ \simeq D_L + D_B f^\circ \tag{33}$$

where f° is the constant fraction of sites in boundaries during the incubation period of recrystallization.

During the rapid increase in crystallite size due to recrystallization, the crystallite growth rate was well represented by the stan-

dard grain growth equation. The fraction of surface covered by boundaries would be the number of boundaries per unit area of film surface multiplied by the boundary width. The fraction of sites in short-circuit paths per unit area at time t would therefore be,

$$f(t) = \frac{2d}{D_t} \tag{34}$$

where d is the boundary width and D_t is the crystallite size at time t. Upon substituting the expression for D_t, obtained from the grain growth equation, equation (26) into equation (32), f becomes,

$$f(t) = \frac{2d}{(D_o^2 + Kt)^{1/2}} \tag{35}$$

The substitution of equation (29) and (35) into (31) gives,

$$\frac{dx}{dt} = \Omega \left\{ D_L \left[1 - \frac{2d}{(D_o^2 + Kt)^{1/2}} \right] + D_B \frac{2d}{(D_o^2 + Kt)^{1/2}} \right\} \frac{\Delta c}{x} \tag{36}$$

Since it is reasonable to assume that boundary diffusion is more rapid than lattice diffusion, $D_B \gg D_L$, equation (36) reduces to,

$$2x \frac{dx}{dt} = 2\Omega D_L \Delta c \left\{ 1 + D_B/D_L \frac{2d}{(D_o^2 + Kt)^{1/2}} \right\} \tag{37}$$

Upon integration, equation (37) yields,

$$x^2 = 2 \Omega D_L \Delta c t \left\{ 1 + D_B/D_L \frac{2d}{K} \frac{2(D_o^2 + Kt)^{+1/2}}{t} \right\} \tag{38}$$

This equation describes the growth of oxide films when both short-circuit and lattice diffusion of the reactants through the film determine

the reaction kinetics. In the absence of short-circuit diffusion in the film, equation (38) reduces to the classical parabolic equation,

$$x^2 = 2\Omega D_L \Delta c t = K_p t \qquad (39)$$

6.3 (ii) Analysis of Data for Oxidation Kinetics

Additional information on the characteristics of nickel short-circuit diffusion in the oxide films may be obtained by combining the above equations with the experimental results of this investigation. These considerations must be confined, however, to films of 600 to 5000Å average thickness whose growth was essentially uniform. It is only in these cases where one could expect diffusion to occur by a random walk process.

The parabolic plots, shown in Figure 40, illustrate that the initial reaction rates approximated parabolic behaviour. While the curves are extended up to 5 hours, only the first 2 hours, shown as solid lines in Figure 40, were calculated by the least squares method. In this time interval the crystallite size was essentially constant, Figure 27.

This stage of film growth may now be analyzed to yield information on the relative magnitudes of boundary and lattice diffusion coefficients. Utilizing equations (29), (32) and (39) the ratio of the effective parabolic rate constant, to the parabolic rate constant for lattice diffusion may be obtained,

$$\frac{K_p(\text{eff})}{K_p} = 1 + D_B/D_L\ f^\circ \simeq D_B/D_L\ f^\circ \qquad (40)$$

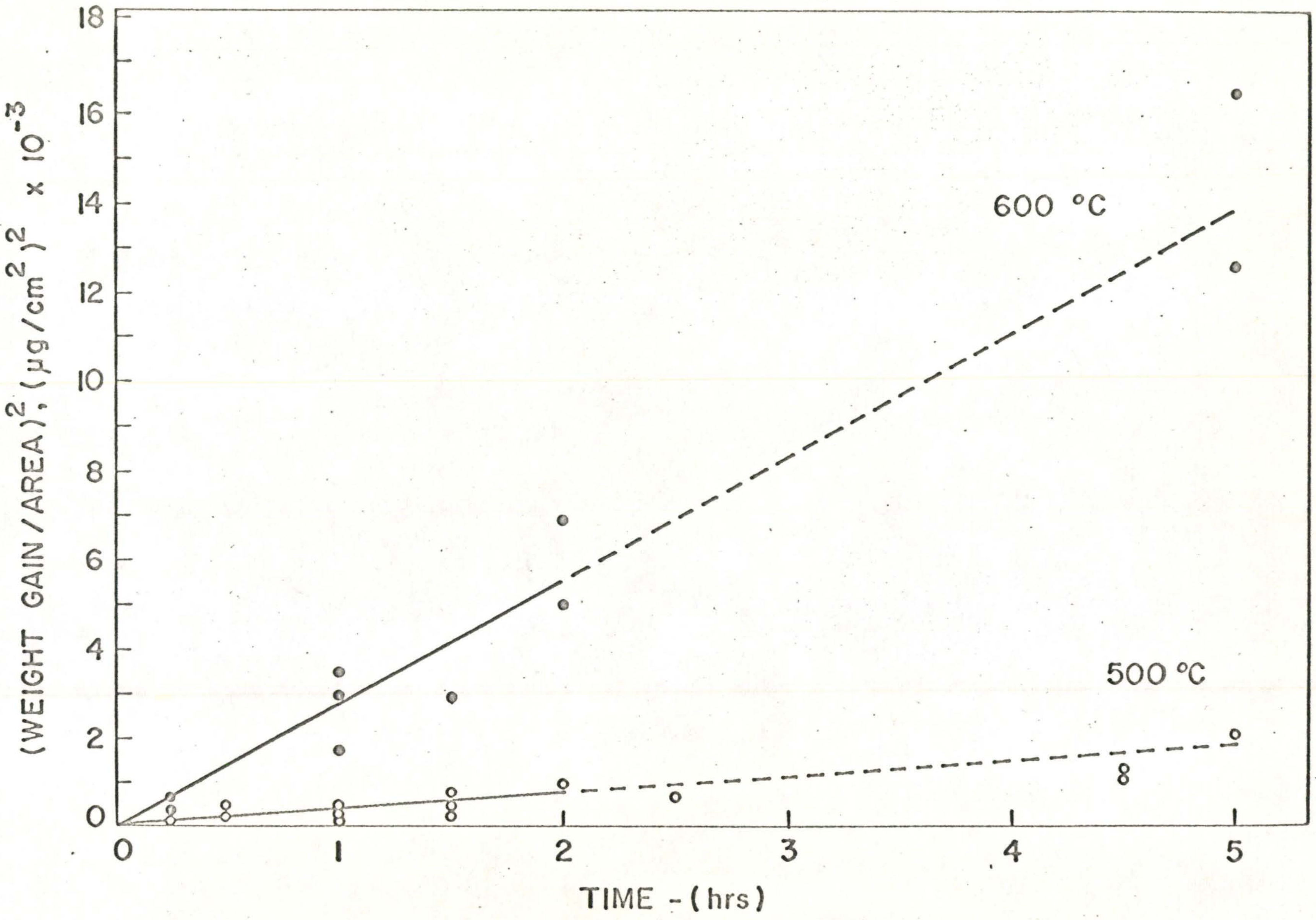

Figure 40: Oxidation kinetics for nickel at 500° and 600°C

For an average crystallite size of 100Å and assuming a boundary width of 10Å, a value of 0.2 was obtained for f° from equation (34). The values for $K_{p(eff)}$ at 500° and 600°C were determined from Figure 40 and equaled 1.0×10^{-13} and 7.8×10^{-13} $(gm/cm^2)^2/sec.$, respectively.

The values for K_p reported in the literature and determined from the values for the self-diffusion coefficient of nickel in nickel oxide by equation (10), are recorded in Table II, along with the corresponding calculated values for D_B/D_L at 500 and 600°C. As to be expected, the boundary diffusion coefficient is much larger than the lattice diffusion coefficient. The ratios lie in range 10^2 to 10^5 and are in agreement with those reported in the literature[60]. Unfortunately, the wide range of values reported in the literature for the lattice diffusion of nickel in nickel oxide, as well as for the parabolic rate constant for the oxidation of nickel, prevented an average value from being assigned to this ratio.

By expressing the ratios of D_B/D_L in the Arrhenius form,

$$D_B/D_L = D_B^\circ/D_L^\circ \exp(E_L-E_B)/RT \qquad (41)$$

the difference in the activation energies for lattice and boundary diffusion were calculated. These values along with those for E_B and the ratios E_B/E_L are also given in Table II. It is to be especially noted, that the values of E_B/E_L range from approximately 0.5 to 0.7, which is in good agreement with those reported in the literature[60].

An additional test of the model was made for films formed at 500°C. This was accomplished by taking tangents to the oxidation curve for 500°C, shown plotted in parabolic form in Figure 41, at times cor-

TABLE II

Ref.	Kp ($gm^2/cm^4/sec$)		D_B/D_L		E_L-E_B	E_L	E_B	E_B/E_L
	500°C	600°C	500°C	600°C	Kcal/mole	Kcal/mole	Kcal/mole	
36	2.30×10^{-15}	5.23×10^{-14}	2.16×10^{2}	0.75×10^{2}	14.2	41.2	27.0	.66
72	6.40×10^{-16}	1.40×10^{-14}	7.75×10^{2}	2.80×10^{2}	13.7	34.7	21.0	.62
51	6.00×10^{-16}	1.08×10^{-14}	8.35×10^{2}	3.65×10^{2}	11.0	38.0	27.0	.71
48	4.2×10^{-16}	1.30×10^{-14}	1.19×10^{3}	3.00×10^{2}	18.4	45.6	27.2	.60
45	2.7×10^{-16}	7.40×10^{-15}	1.85×10^{3}	5.30×10^{2}	16.5	44.2	27.7	.63
47	2.4×10^{-17}	8.80×10^{-16}	2.09×10^{4}	4.45×10^{3}	20.6	48.4	27.8	.58
46	4.0×10^{-18}	3.00×10^{-16}	1.25×10^{5}	1.30×10^{4}	30.2	56.0	25.8	.46

TABLE III

Oxidation Time (hrs.)	Measured Crystallite Size (Å)	Calculated Crystallite Size (Å)
4	560	280
8	675	370
13	845	500

responding to those for which average crystallite sizes were determined. The tangents, K_t, are equivalent to the instantaneous reaction rate constant at those times. In a similar manner to that used to derive equation (40), it can be shown that,

$$\frac{K_t}{K_p} = 1 + D_B/D_L\ f(t) \simeq D_B/D_L\ f(t) \qquad (42)$$

where f(t) is the fraction of sites within boundaries at time t.

From equation (42) the following expression was derived,

$$\frac{K_t}{K_t^\circ} \simeq \frac{D_B/D_L\ f(t)}{D_B/D_L\ f^\circ} = \frac{f(t)}{f^\circ} = \alpha = \frac{D_o}{D_t} \qquad (43)$$

where K_t° is the limiting tangent as time approaches zero, D_o is the initial crystallite size and D_t is the crystallite size at time t.

The values of K_t were determined from tangents to the curve shown in Figure 41. These calculated values are given in Table III, along with the experimentally measured values. The calculated crystallite sizes are not less than one-half the measured values. This is reasonable agreement within the limitations of the experimental accuracy of the kinetic data and the determinations of crystallite sizes. Similar calculations were not carried out for 600°C since sufficient experimental data, preceding the formation of non-uniform films, was not available.

The results of this analysis, for the evaluations of the ratios of the diffusion coefficients D_B/D_L, the activation energy ratios E_B/E_L and the calculations of crystallite sizes from the oxidation curve at 500°C, all support the validity of the assumptions based upon lattice

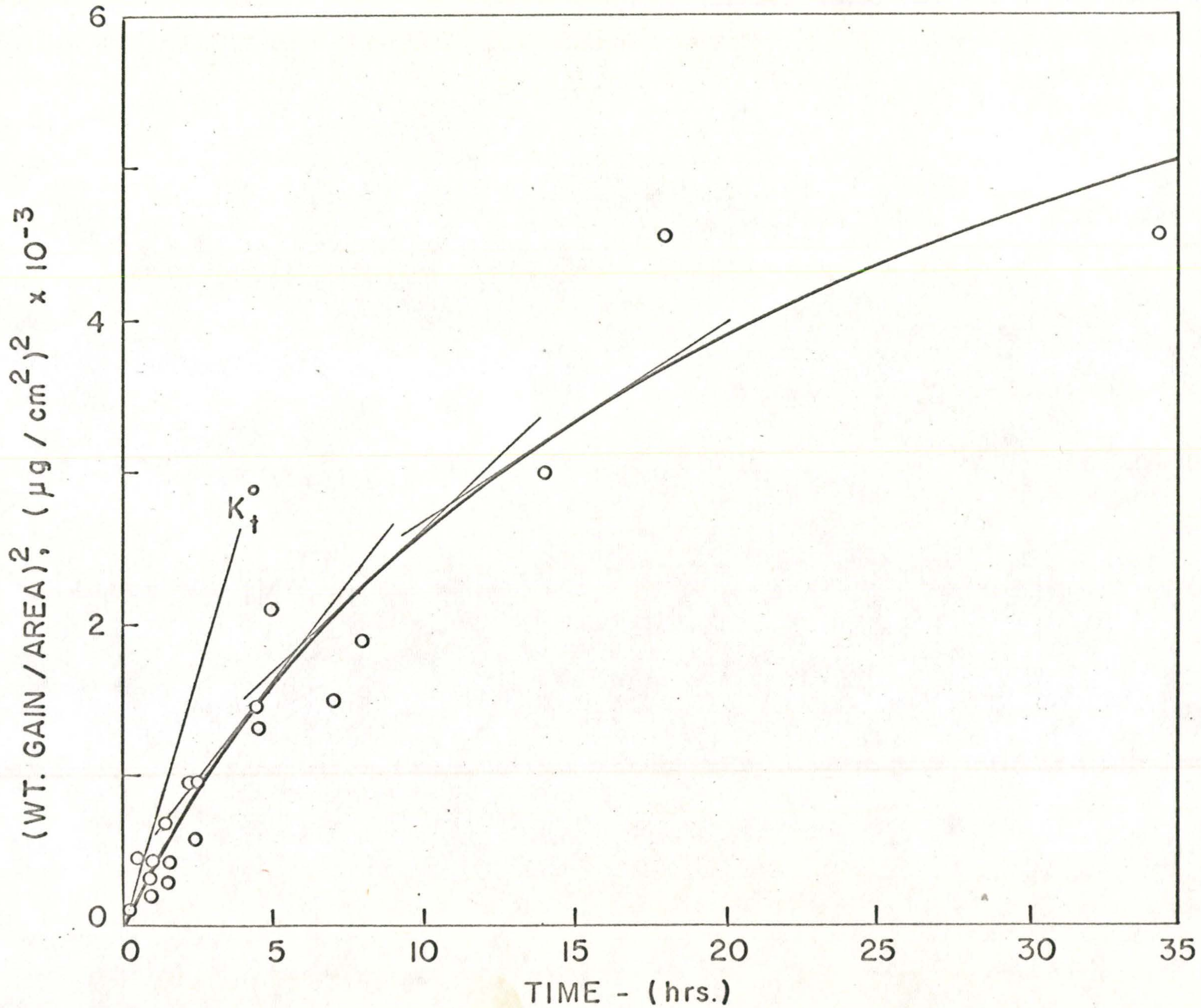

Figure 41: Oxidation kinetics for nickel at 500°C

and short-circuit diffusion of nickel in the oxide films. Furthermore, the value of 19 Kcal/mole calculated for the activation energy for boundary migration is in good agreement with the values of 21-28 Kcal/mole calculated for boundary diffusion.

There are, however, serious limitations to the above analysis and assumptions for the oxidation film model. It was assumed, that the kinetics determined by oxide weight gain measurements defined a uniform film over the entire metal specimen. However, the results obtained from transmission electron microscopy clearly revealed that the films were only uniform on individual metal grains. Consequently, an averaging process has been assumed for the analysis of the data for oxidation kinetics. This assumption appeared to give a good approximation because of the large number of grains constituting the polycrystalline metal sample. Also, triplicate oxidation tests showed a maximum deviation of less than ± 27 per cent in the early stages of the reaction.

In the derivation of equations based on the proposed oxide film model, all crystallite boundaries were assumed to be equivalent short-circuit diffusion paths. This approximation was made in order to obtain a tractable mathematical expression for the growth kinetics. As pointed out in the first section of this chapter, the effectiveness of crystallite boundaries to transport material by short-circuit diffusion depends on the misorientation of the crystallites. Transmission electron microscopy showed that the misorientation of the crystallites was different on different metal grains, Figures 12-15, and that it decreased with increasing oxidation for a given film orientation, Figure 16. In addition to the fact that differences in crystallite misorientation were

not considered, all of the crystallite size determinations were made on films of only one orientation. Thus, the correlation obtained between the oxidation kinetics of the polycrystalline metal and recrystallization and grain growth process occurring in the oxide film must be regarded as only a first approximation to a system exhibiting complex reaction parameters.

6.3 (iii) The Growth of Non-Uniform Oxide Films

In all cases where non-uniform growth was observed the films were no longer composed of small oxide crystallites. Instead, the films consisted of large grains whose thickness was equal to that of the oxide film and whose area was approximately the same as the original metal grains, Figures 30 and 31. In the thinner areas of these films it was possible to distinguish dislocations and their distribution varied from a random arrangement, Figure 29, to well defined sub-boundaries, Figure 34. Since only a limited number of non-uniform films were examined in this investigation, the structural changes which occurred can only be described qualitatively.

The two most salient features of the structure of the films at this stage of the oxidation process were the high density of dislocations and the large grain size. Although no direct observations were obtained concerning the growth of the large grains it seems reasonable to postulate that they resulted from the preferential migration of some highly mobile boundaries as occurs in conventional recrystallization processes in metals[73].

The high density of dislocations in the films may have occurred as a consequence of the stresses generated by the volume difference

between the oxide and the substrate (1:1.65 for nickel and nickel oxide). The dislocation density of $10^{10}/cm^2$ calculated for the oxide film shown in Figure 29 is similar to the densities reported by Pashley[(74)] for the epitaxial growth of thin metallic films on non-metallic substrates. In order to reduce the total energy of the system the dislocations can be arranged by climb and glide processes into well defined sub-boundary walls[(75)] such as shown in Figure 34. Such rearrangements would be expected to occur at the temperatures and times involved in the oxidation process.

As previously discussed, the short-circuit diffusion of nickel across the film via dislocations, resulted in preferential film growth in the neighbourhood of dislocations oriented approximately perpendicular to the plane of the film. As would be expected, on the basis of the above argument, the films which contained well defined dislocation networks were the most uneven in thickness, Figure 30. As shown in Figure 35, thickening of the oxide film has occurred overlying sub-boundaries oriented perpendicular to the plane of the film. If it is assumed that the film thickness was 5000Å in the thin areas of this 8000Å thick film formed at 600°C, then nearly all of the dislocation networks which appeared in good contrast, as shown in Figure 34, were inclined at less than 20 degrees with the plane of the film.

CHAPTER VII

Suggestions for Further Work

1) Many of the limitations to the proposed oxide film model may be avoided by carrying out an investigation, similar to that described in this thesis, on single crystal nickel samples. This would eliminate the averaging process which must be assumed for polycrystalline material. The oxide film thicknesses and oxidation kinetics could be more accurately determined, as well as the relationships between average crystallite size and oxidation time and film thickness. In addition, by monitoring the decrease in misorientation between crystallites during the early stages of oxide growth, when no change in crystallite size was detected, and by comparing results from nickel crystals of different orientations, information may be obtained concerning the relationship between crystallite misorietation and short-circuit diffusion via crystallite boundaries. Such information would permit further refinements to the present film model in which all boundaries have been treated as equivalent short-circuit diffusion paths.

2) More observations are necessary in order to describe in greater detail the transition from a film composed of small crystallites to one consisting of large oxide grains. The present investigation has indicated that this can best be accomplished by working at the higher temperatures of 700° and 800°C. At these temperatures the transition occurred at film thicknesses of less than 1000Å making these films more suitable for transmission electron microscopy.

3) Direct measurements are required to determine the magnitude of the effective diffusion coefficient for nickel in nickel oxide films of different crystallite sizes and dislocation distributions. The radioactive isotope nickel-63 could be useful in making this determination.

CHAPTER VIII

Conclusions

1) Thin nickel oxide films formed on nickel at 500° and 600°C varied both in thickness and orientation from one metal grain to another.

2) Varying degrees of preferential oxidation occurred overlying the original metal grain boundaries but not at twin boundaries.

3) The oxide films were composed of numerous small irregular shaped oxide crystallites for average film thicknesses up to at least 3500 and 5000Å, formed at 500° and 600°C, respectively.

4) For a given average film thickness the misorientation between crystallites was less for the thinner areas while the crystallite size was approximately the same for both thin and thick regions.

5) For a given film orientation, the oxide crystallites increased in size with increased oxidation time and the misorientation between the crystallites decreased.

6) The increase in crystallite size was controlled by recrystallization and grain growth occurring in the oxide films.

7) An oxide film model has been advanced which correlates the initial oxidation kinetics with simultaneous lattice diffusion and short-circuit diffusion of nickel via oxide crystallite boundaries.

8) At a later stage in the oxidation process, the preferential migration of some boundaries resulted in the formation of large oxide grains. These films contained dislocations, whose distribution varied from a random arrangement to well defined sub-boundaries.

9) The short-circuit diffusion of nickel via dislocations or sub-boundaries, oriented approximately perpendicular to the plane of the film, resulted in non-uniform film growth.

BIBLIOGRAPHY

1. Evans, U. R., The Corrosion and Oxidation of Metals, London: Edward Arnold, (1960).
2. Kubaschewski, O., and Hopkins, B. E., Oxidation of Metals and Alloys, London: Butterworths, (1962).
3. Hauffe, K., Oxidation of Metals, New York: Plenum, (1965).
4. Benard, J., Oxidation des Metaux, Paris: Gauthier-Villars, 1962-1964, (2V.).
5. Seybolt, A. U., Advances in Physics, 12, 1 (1963).
6. Mott, N. F., Trans. Faraday Soc., 36, 472 (1940).
7. Hauffe, K., and Ilschener, B., Z. Elektrochem., 58, 467 (1954).
8. Cabrera, N., and Mott, N. F., Rept. Progr. Phys., 12, 163 (1948-49).
9. Grimley, T. B., and Trapnell, B. M. W., Proc. Roy. Soc. (London), A234, 405 (1956).
10. Uhlig, H., Pickett, J., and Macnairn, J., Acta Met., 7, 111 (1959).
11. Landsberg, P. T., J. Chem. Phys., 23, 1079 (1955).
12. Tammann, G., Z. anorg. Chem., 111, 78 (1920).
13. Pilling, N. B., and Bedworth, R. E., J. Inst. Met., 29, 529 (1923).
14. Wagner, C., Z. Phys. Chem., (B), 21, 25 (1933).
15. Wagner, C., Atom Movements, A.S.M., Cleveland, p. 153 (1951).
16. Bardolle, J., and Bénard, J., Compt. rend., 232, 231 (1951).
17. Gulbransen, E. A., MacMillan, W. R., and Andrew, K. F., Trans. AIME, 6, 1027 (1954).

18. Harris, W., Ball, F. R., and Gwathmey, A. T., Acta Met., 5, 574 (1957).

19. Phelps, R. T., Gulbransen, E. A., and Hickman, J. W., Industr. Engng. Chem. (Anal.), 18, 391 (1946).

20. Sewell, P. B., Brewer, E. G., and Cohen, M., Proceedings, Fifth International Congress for Electron Microscopy, Academic Press, N.Y., (1962).

21. Douglass, D. L., and Van Landuyt, J., Acta Met. 14, 491 (1966).

22. Shewman, P. G., Diffusion in Solids, New York: McGraw-Hill, (1963).

23. Evans, U. R., The Corrosion and Oxidation of Metals, London: Edward Arnold p. 833 (1960).

24. Davies, D. E., Evans, U.R., and Agar, J. N., Proc. Roy. Sec. (London), A225 (1954).

25. Harrison, P. L., J. Electrochem. Soc., 112, 235 (1965).

26. Meijering, J. L., and Verheijke, M. L., Acta Met., 7, 331 (1959).

27. Smeltzer, W. W., Haering, R. R., and Kirkaldy, J. S., Acta Met., 9, 880 (1961).

28. Irving, B. A., Corros. Sci. 5, 471 (1965).

29. Fisher, J. C., J. Appl. Phys., 22, 74 (1951).

30. Whipple, R. T. P., Phil. Mag., 45, 1225 (1954).

31. Turnbull, D., and Hoffman, R. E., Acta Met. 2, 419 (1954).

32. Hart, E. W., Acta Met., 5, 597 (1957).

33. Ruoff, A. L., and Balluffi, R. W., J. Appl. Phys., 34, 1848 (1963).

34. Wood, G. C., Wright, I. G., and Ferguson, J. M., Corros. Sci., 5, 645 (1965).

35. A.S.M. Metals Handbook, Cleveland: ASM, (1948).

36. Gulbransen, E. A., and Andrew, K. F., J. Electrochem. Soc. 101, 128 (1954).

37. Gulbransen, E. A., and Hickman, J. W., Trans. AIME, 171, 306 (1947).

38. Arkharoff, V. I., and Graevsky, K. M., Z. Tekh. fiz, 14, 132 (1944).

39. Hansen, M., and Anderko, K., Constitution of Binary Alloys, New York: McGraw-Hill, 1958, p. 1024.

40. Tylecote, R. F., J. Iron and Steel Inst., 196, 135 (1960).

41. Verwey, M., Haaijman, M., Romeijnan, H., and von Osterterhout, M., Philips Research Repts., 5, 173 (1950).

42. Mitoff, S. P., J. Chem. Phys., 35, 882 (1961).

43. Baur, J. P., Bartlett, R. W., Ong, Jr., J.N., and Fassell, Jr., W. M., J. Electrochem. Soc., 110, 185 (1963).

44. Morin, F. J., Phys. Rev., 93, 1199 (1954).

45. Shim, M. T., and Moore, W. J., J. Chem. Phys., 26, 802 (1957).

46. Lindner, R., and Akerström, A., Discussions Faraday Soc., 23, 133 (1957).

47. Klotsman, S. M., Timofeyev, A. N., and Trakhtenberg, I. Sh., Fiz. metal. metalloved., 14, 428 (1962).

48. Choi, J. S., and Moore, W. J., J. Phys. Chem., 66, 1308 (1962).

49. O'Keefe, M., and Moore, W. J., J. Phys., Chem., 65, 1438 (1961).

50. Kubaschewski, O., and Hopkins, B. E., Oxidation of Metals and Alloys, London: Butterworth, p. 144 (1962).

51. Philipps, W. L., J. Electrochem. Soc., 110, 1014 (1963).

52. Gulbransen, E. A., and Andrew, K. F., J. Electrochem. Soc., 104, 451 (1957).

53. Engell, H. J., Hauffe, K., and Ilschner, B., Z. Elektrochem., 58, 478 (1954).

54. Martius, U., Can. J. Phys., 35, 466 (1955).

55. Lawless, K. R., Young, F. W., and Gwathmey, A. T., J. Chim. Phys., 53, 667 (1956).

56. Collins, L. E., and Heavens, O. S., Proc. Phys. Soc. 70B, 265 (1957).

57. Newkirk, J. B., and Martin, W. G., Trans. Amer. Inst. Mech. Engrs., 212, 398 (1958).

58. Otter, M., Z. Naturf, 14A, 355 (1959).

59. Pu, H., Chien-ti, C., and Ke-hsin, K., Scientia Sinica, 14, 632 (1965).

60. Mclean, D., Grain Boundaries in Metals, Oxford: Clarendon, 1957, p224.

61. Hirano, K. I., Agarwala, R. P., and Cohen, M., Acta. Met., 10, 857 (1962).

62. Hirsch, P. B., Howie, A., Nicholson, R. B., Pashley, D. W., and Whelan, M. J., Electron Microscopy of Thin Crystals, London: Butterworths, 1965.

63. ibid. p.128.

64. Heidenreich, R. D., Fundamentals of Transmission Electron Microscopy, New York: Interscience, 1965, p.375.

65. ibid. p.178.

66. Cahn, R. W., Physical Metallurgy, New York: Interscience, 1965, p. 939.

67. Burk, J. E., and Turnbull, D., Prog. Met. Phys., 3, 220 (1961).

68. Beck, P. A., J. Appl. Phys., 19, 507 (1948).

69. Mott, N. F., Proc. Phys. Soc., 60, 391 (1948).

70. Detert, K., and Dressler, G., Acta Met. 9, 653 (1965).

71. Fick, A., Pogg. Ann., 94, 59 (1855).

72. Moore, W. J., and Lee, J. K., Trans. Farad. Soc., 48, 916 (1952).

73. Cahn R. W., Physical Metallurgy, New York: Interscience, 1965 p 977.

74. Pashley, D. W., The Growth and Structure of Thin Films, Cleveland: A.S.M., 1963, p 59.

75. Li, J. C. M., J. Appl. Phys., 32, 525 (1961).